Inclusive search for Long-lived light neutralino in B decays with baryonic R-parity violation at Belle II

A Thesis submitted for the completion of requirements for the degree of

Master of Science
(Research)

by

Tasmay Goswami
Undergraduate Programme
Indian Institute of Science

भारतीय विज्ञान संस्थान

Under the supervision of

Dr. Minakshi Nayak
Centre for High Energy Physics, Indian Institute of Science

Declaration

I, **Goswami Tasmay Mehulgiri**, declare that this project titled, *"Inclusive search for Long-lived light neutralino in B decays with baryonic R-parity violation at Belle II"* and the work presented in it are my own. I confirm that:

- This work was done wholly or mainly while in candidature for a research degree at this University.
- Where any part of this thesis has previously been submitted for a degree or any other qualification at this University or any other institution, this has been clearly stated.
- Where I have consulted the published work of others, this is always clearly attributed.
- Where I have quoted from the work of others, the source is always given. With the exception of such quotations, this thesis is entirely my own work.
- I have acknowledged all main sources of help.
- Where the thesis is based on work done by myself jointly with others, I have made clear exactly what was done by others and what I have contributed myself.

Name: Goswami Tasmay Mehulgiri

Signed:

CERTIFICATE

This is to certify that the Master's project titled *"Inclusive search for Long-lived light neutralino in B decays with baryonic R-parity violation at Belle II"* submitted by **Goswami Tasmay Mehulgiri** (Sr No. 11-01-00-10-91-21-1-20617) to Indian Institute of Science, Bangalore towards partial fulfilment of requirements for the award of degree of Master of Science (Research) in Physics is a record of bona fide work carried out by him under my supervision and guidance during Academic Year 2025-26.

Signature of the faculty

Name of the faculty: Minakshi Nayak

Minakshi Nayak

Department: Centre for High Energy Physics, IISc Bangalore, India

Name of the faculty: Sudhir Vempati

Department: Centre for High Energy Physics, IISc Bangalore, India

Abstract

We investigate the prospects of searching for a light, long-lived neutralino in a baryon-number-violating R-parity violating supersymmetric framework at the Belle II experiment. In this scenario, a GeV-scale bino-like neutralino is produced in B-meson decays and subsequently decays into hadronic final states with a macroscopic lifetime, leading to displaced vertex signatures inside the detector.

An inclusive search strategy is adopted, targeting multi-track displaced vertices without requiring full reconstruction of specific decay modes. This approach enhances sensitivity by capturing a broad class of signal topologies while it definitely requires strong background suppression. The analysis is carried out within the Belle II analysis software framework, focusing on the suppression of Standard Model backgrounds using displaced track parameter variables and vertex-level observables. Building on existing phenomenological study, which indicate that Belle II can probe neutralino masses in the range of 2.7–4.3 GeV under the assumption of supressed background, this work aims to develop and optimize selection strategies to achieve such background suppression in a realistic experimental setting.

Contents

Introduction and Motivation

The Standard Model (SM) of particle physics provides an extremely successful description of fundamental interactions, yet it leaves several key questions unanswered, including the nature of dark matter, the origin of the baryon asymmetry of the Universe, and the absence of new physics at the electroweak scale. These open problems motivate the exploration of physics beyond the Standard Model (BSM), with supersymmetry (SUSY) being one of the most well-studied extensions.

In conventional SUSY scenarios, R-parity conservation is imposed to ensure the stability of the lightest supersymmetric particle (LSP), often making it a viable dark matter candidate. However, R-parity violation (RPV) provides an alternative framework in which baryon- or lepton-number-violating interactions are allowed. In particular, baryon-number-violating (BNV) RPV scenarios permit the existence of a light, GeV-scale neutralino that is not stable and can decay into Standard Model particles.

Such a light neutralino can be produced in rare B-meson decays via RPV couplings, for example through processes of the form

$$B^+ \to p\,\tilde{\chi}_1^0. \tag{1}$$

The neutralino subsequently decays into hadronic final states via a second RPV coupling. Due to the suppression of the decay width by small RPV couplings and heavy squark masses, the neutralino can acquire a macroscopic lifetime, leading to displaced decays inside the detector volume.

These displaced decays result in distinctive displaced vertex (DV) signatures, which are experimentally clean and provide strong discrimination against prompt SM backgrounds. As a result, long-lived particles (LLPs) have become an important target in the search for new physics, especially in light of the absence of signals in conventional high-energy searches.

The Belle II experiment, operating at the SuperKEKB e^+e^- collider, offers a unique environment for probing such scenarios. Its clean collision environment, excellent tracking resolution, and large dataset of B-meson decays make it particularly sensitive to light, weakly coupled particles with displaced signatures.

Search strategies for such neutralinos can be broadly classified into two categories: exclusive and inclusive approaches. Exclusive searches aim to fully reconstruct specific decay channels of the neutralino, but suffer from limited sensitivity due to small branching fractions and reconstruction inefficiencies. In contrast, inclusive searches target generic displaced vertex signatures without requiring full reconstruction of the decay chain, thereby accessing a significantly larger fraction of signal events.

Phenomenological studies have shown that an inclusive displaced-vertex search at Belle II can improve sensitivity by up to an order of magnitude compared to exclusive approaches, potentially probing neutralino masses in the range of 2.7–4.3 GeV, provided that Standard Model backgrounds are sufficiently suppressed [1]. This highlights the importance of developing robust background rejection strategies in realistic experimental conditions.

In this thesis, we focus on implementing an inclusive search strategy for long-lived neutralinos at Belle II. The primary objective is to construct and optimize a displaced vertex reconstruction and selection framework within the Belle II analysis software, with particular emphasis on suppressing backgrounds arising from prompt tracks, secondary decays, and hadronic interactions in detector material. This work aims to bridge the gap between phenomenological sensitivity projections and a practical analysis framework capable of achieving the required level of background suppression.

Chapter 1

Supersymmetry and Minimal SUSY Standard Model

1.1 Limitations of the Standard Model

The Standard Model (SM) of particle physics provides an exceptionally successful description of fundamental particles and their interactions, with predictions that have been experimentally verified to remarkable precision. Despite this success, it is widely understood to be incomplete. Several conceptual and phenomenological issues remain unresolved.

A central theoretical issue is the hierarchy problem, which arises from the quadratic sensitivity of the Higgs boson mass to ultraviolet physics. Radiative corrections to the Higgs mass scale with the square of the cutoff, requiring a high degree of fine-tuning to maintain the electroweak scale. In addition, the Standard Model does not provide a viable candidate for dark matter, whose existence is strongly supported by astrophysical and cosmological observations. The running of gauge couplings also fails to unify precisely at a high scale within the SM, and neutrino masses cannot be accommodated without extending the particle content.

These limitations strongly motivate extensions of the Standard Model. Supersymmetry (SUSY) is among the most theoretically compelling proposals, as it addresses several of these issues within a unified framework.

Supersymmetry: A Boson-Fermion Symmetry

To address these gaps, SUSY postulations begin with a fundamental expansion of the Poincaré algebra. Supersymmetry introduces a symmetry between fermions and bosons, relating particles of different spin through fermionic generators Q. These generators satisfy the algebra

$$\{Q, \bar{Q}\} \sim P^\mu, \tag{1.1}$$

where P^μ is the four-momentum operator. As a consequence, each Standard Model particle is associated with a superpartner differing in spin by one-half unit.

Quarks and leptons acquire scalar partners known as squarks and sleptons, while gauge bosons are accompanied by fermionic partners called gauginos. The Higgs sector is similarly extended to include fermionic higgsinos. Since none of these superpartners have been observed at current collider energies, supersymmetry must be a broken symmetry, with superpartners acquiring masses above the electroweak scale.

1.2 Supersymmetry and the Hierarchy Problem

The introduction of these superpartners is not merely an exercise in symmetry; it provides a direct mechanism to resolve the technical naturalness of the theory. One of the primary motivations for supersymmetry is its ability to stabilize the Higgs mass against large radiative corrections. In the Standard Model, loop corrections to the Higgs mass squared scale as

$$\delta m_H^2 \sim \frac{\Lambda^2}{16\pi^2}, \tag{1.2}$$

where Λ is the ultraviolet cutoff. This leads to the well-known naturalness problem, as maintaining a light Higgs mass requires delicate cancellations between large contributions.

In a supersymmetric theory, contributions from fermionic and bosonic loops enter with opposite signs. For example, the quadratic divergence from the top quark loop is cancelled by the corresponding scalar top (stop) loop. As a result, the correction becomes sensitive only to the mass splitting between superpartners,

$$\delta m_H^2 \propto m_{\tilde{t}}^2 - m_t^2. \tag{1.3}$$

This cancellation ensures that the Higgs mass remains stable provided the superpartner masses are not too far above the electroweak scale.

1.3 Particle Content of the MSSM

Building upon these symmetry principles, we arrive at a concrete particle spectrum. The Minimal Supersymmetric Standard Model (MSSM) is the simplest realization of supersymmetry consistent with the Standard Model gauge structure. In this framework, each SM field is embedded into a supermultiplet containing both fermionic and bosonic degrees of freedom.

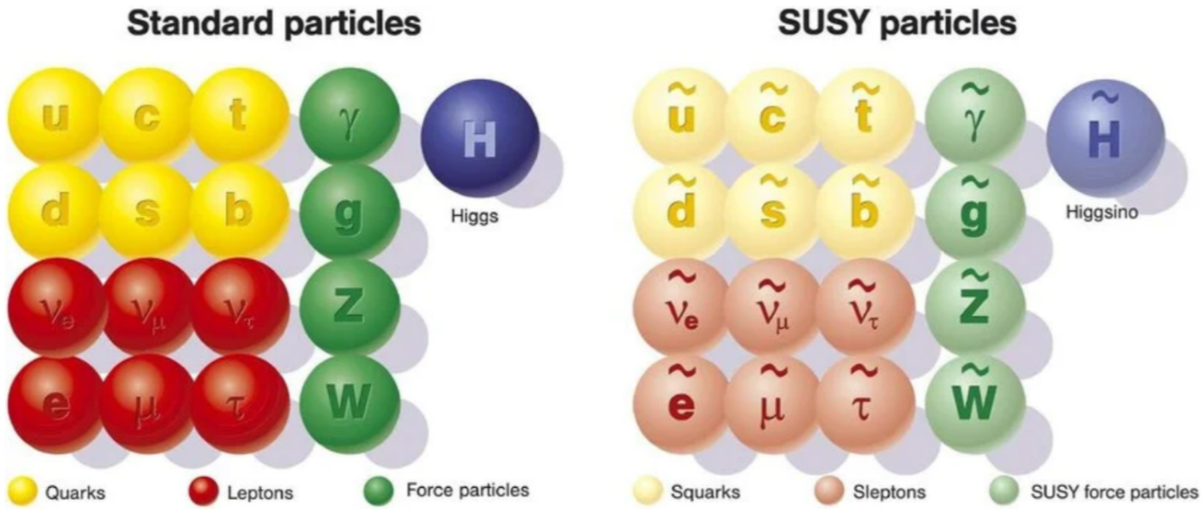

Figure 1.1: Particle content of the Standard Model and their supersymmetric partners in the MSSM.

The matter sector is extended by introducing scalar partners for all quarks and leptons, while the gauge sector includes fermionic gauginos associated with each gauge boson. The Higgs sector requires particular modification: instead of a single Higgs doublet, the MSSM contains two Higgs doublets, H_u and H_d. This structure is necessary to generate masses for both up-type and down-type fermions while maintaining gauge invariance and anomaly cancellation.

Supermultiplets and SUSY Structure

The organization of this expanded particle content is governed by the mathematical structure of supermultiplets. Supersymmetric theories are formulated in terms of supermultiplets, which group together fields related by SUSY transformations. These multiplets provide a natural organizational framework for the particle content.

Chiral supermultiplets contain a Weyl fermion and a complex scalar field. They describe matter fields such as quarks and leptons, as well as the Higgs fields. Gauge supermultiplets, on the other hand, contain a gauge boson and its fermionic partner, the gaugino. These structures ensure that supersymmetry transformations map bosonic degrees of freedom to fermionic ones and vice versa, preserving the symmetry of the theory.

R-parity

While the MSSM framework defines the particles, their stability and interaction signatures are determined by additional discrete symmetries. A discrete symmetry known as R-parity is often imposed in the MSSM to control baryon- and lepton-number violating processes. It is defined as

$$R_p = (-1)^{3(B-L)+2s}. \tag{1.4}$$

Under this symmetry, all Standard Model particles have $R_p = +1$, while their supersymmetric partners carry $R_p = -1$. If R-parity is conserved, supersymmetric particles must be produced in pairs, and the lightest supersymmetric particle is stable. This has important phenomenological consequences, particularly in the context of dark matter searches.

Connection to This Work

Moving beyond the standard assumptions of R-parity conservation, this thesis explores the phenomenological possibilities of a broken symmetry. In this work, we consider a scenario in which the lightest neutralino is light, with a mass in the GeV range, and long-lived due to suppressed R-parity violating couplings. Such a particle can be produced in rare B-meson decays and subsequently decay into hadronic final states at a displaced location within the detector.

This motivates a search strategy based on topology of the decay process, which is explained in detail in the following chapters. The theoretical framework governing neutralino production and decay is presented in Chapter 2, followed by a description of the Belle II detector in Chapter 3 and the experimental methodology used in this analysis in Chapter 4.

Chapter 2

Theoretical Framework

2.1 Light Neutralino in R-parity Violating Supersymmetry

The general principles of SUSY and R-parity discussed in the previous chapter provide the foundation for a specific, detectable scenario involving R-parity violation (RPV).

Supersymmetry and Neutralinos

In the Minimal Supersymmetric Standard Model (MSSM), the fermionic superpartners of the neutral electroweak gauge bosons and Higgs bosons mix to form four neutral mass eigenstates known as neutralinos.

In the gauge eigenstate basis $(\tilde{B}, \tilde{W}^0, \tilde{H}_u^0, \tilde{H}_d^0)$, the neutralino mass matrix is given by [2]:

$$\mathcal{M}_{\tilde{\chi}^0} = \begin{pmatrix} M_1 & 0 & -m_Z \sin\theta_W \cos\beta & m_Z \sin\theta_W \sin\beta \\ 0 & M_2 & m_Z \cos\theta_W \cos\beta & -m_Z \cos\theta_W \sin\beta \\ -m_Z \sin\theta_W \cos\beta & m_Z \cos\theta_W \cos\beta & 0 & -\mu \\ m_Z \sin\theta_W \sin\beta & -m_Z \cos\theta_W \sin\beta & -\mu & 0 \end{pmatrix}. \tag{2.1}$$

Diagonalization of this matrix yields four neutralino states $\tilde{\chi}_i^0$ $(i = 1, 2, 3, 4)$. In many phenomenological scenarios, the lightest neutralino, $\tilde{\chi}_1^0$, is predominantly bino-like, with its mass primarily determined by the soft SUSY-breaking parameter M_1. In this work, $\tilde{\chi}_1^0$ is treated as the lightest supersymmetric particle (LSP) with a mass in the range of a few GeV [1].

R-parity and Its Violation

In the MSSM, a discrete symmetry known as R-parity is often imposed to prevent rapid proton decay. It is defined as [3]:

$$R_p = (-1)^{3(B-L)+2s}, \tag{2.2}$$

where B and L denote baryon and lepton numbers, respectively, and s is the particle spin.

While R-parity conservation requires that supersymmetric particles are produced in pairs and the LSP is stable, it is not a fundamental theoretical requirement. Allowing R-parity violation (RPV) introduces additional terms in the superpotential. Of particular relevance to this study are baryon-number-violating (BNV) operators of the form [3]:

$$\mathcal{W}_{\text{RPV}} \supset \lambda''_{ijk}\, \bar{U}_i \bar{D}_j \bar{D}_k, \tag{2.3}$$

where λ''_{ijk} are dimensionless couplings and i, j, k are generation indices. These operators enable interactions involving three quarks, facilitating both the single production and subsequent decay of the neutralino.

2.2 Neutralino Production and Decay Dynamics

Under the RPV framework, the neutralino is no longer an invisible, stable particle, but a source of unique experimental signatures.

2.2.1 Production in B-meson Decays

In BNV RPV scenarios, a light neutralino can be produced in rare B-meson decays. Assuming the production is mediated by a coupling such as λ''_{113} [1], a representative production channel is:

$$B^+ \to p\, \tilde{\chi}_1^0. \tag{2.4}$$

The presence of a baryon in the final state is a direct consequence of baryon-number violation. This process is mediated by a virtual squark, which enables the transition between the initial-state quarks and the final-state baryon and neutralino (see Fig. 2.1), Such decay modes are particularly relevant for the Belle II experiment, which produces large samples of B mesons at the $\Upsilon(4S)$ resonance. Depending on the flavor structure of the RPV coupling, different baryonic final states such as protons, neutron, and strange baryons $(\Lambda, \Sigma, \Xi\ )$ can be produced.

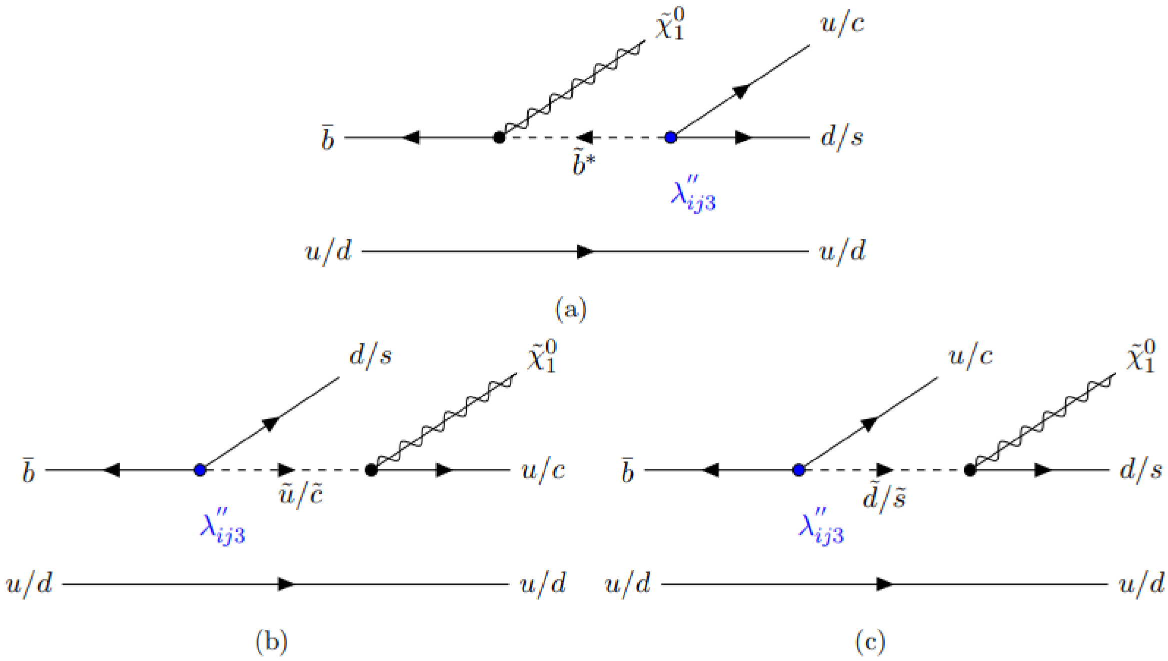

Figure 2.1: Parton-level diagrams for the decays $B^{+/0} \to Baryon + \tilde{\chi}_1^0$, are shown with the corresponding RPV coupling λ''_{ij3}. The possible baryons are: p, n (for λ''_{113}); $\Lambda, \Sigma^+, \Sigma^0$ (for λ''_{123}); $\Lambda_c^+, \Sigma_c^+, \Sigma_c^0$ (for λ''_{213}); and Ξ_c^+, Ξ_c^0 (for λ''_{223}), [1]

2.2.2 Neutralino Decay Channels and Lifetimes

Following its production, the neutralino decays via a second non-zero RPV coupling (e.g., λ''_{212}) into three quarks at the parton level [1]:

$$\tilde{\chi}_1^0 \to c\, s\, d. \tag{2.5}$$

This decay proceeds via the exchange of a virtual squark (Fig. 2.2). At energies relevant for Belle II, this interaction is accurately described using an effective four-fermion operator obtained after integrating out the heavy squark propagators.

The decay width of the neutralino is heavily suppressed by both the smallness of the RPV couplings and the large mass of the intermediate squarks. Parametrically, the decay width scales as [3]:

$$\Gamma \sim \frac{|\lambda''|^2}{m_{\tilde{q}}^4}\, m_{\tilde{\chi}_1^0}^5. \tag{2.6}$$

As a consequence, the neutralino can have a macroscopic decay length ranging from millimeters to meters, thereby classifying it as a long-lived particle (LLP). This long lifetime is a key feature that determines its experimental observability.

Based on available phase space and hadronization dynamics, phenomenological studies [1] identify several dominant primary decay channels:

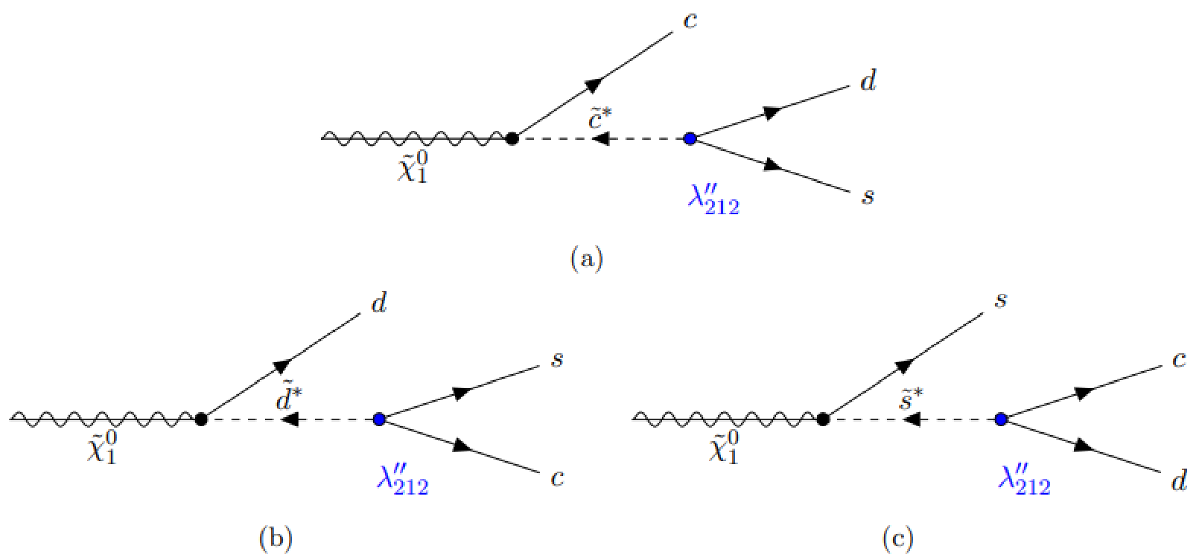

Figure 2.2: Parton-level diagrams for the decay $\tilde{\chi}_1^0 \to csd$ induced by RPV SUSY coupling λ''_{212}, [1]

- $\tilde{\chi}_1^0 \to \Lambda_c^+ K^-$
- $\tilde{\chi}_1^0 \to \Sigma_c K$
- $\tilde{\chi}_1^0 \to \Xi_c \pi$

These primary charmed baryons subsequently decay into lighter hadrons, cascading into final states with multiple charged tracks. The exact track multiplicity depends on the neutralino mass; four-track final states dominate at lower masses, while six-track modes become accessible as heavier intermediate states are kinematically allowed.

Hadronization Modelling with `Pythia8` and Herwig

To model these signatures realistically, hadronization and final-state particle production are simulated using the `Pythia8` and HERWIG event generators. Their respective string fragmentation and cluster hadronization models provide a comprehensive description of track multiplicities and kinematic distributions, enabling an inclusive analysis of multi-track displaced vertices without restricting the study to specific exclusive decay channels. Further details are discussed in Chapter 5.

Chapter 3

The Belle II Detector

3.1 Overview of the Belle II Experiment

The Belle II detector [4, 5] is a general-purpose magnetic spectrometer operating at the SuperKEKB asymmetric electron–positron collider [6], located at the KEK laboratory in Tsukuba, Japan. SuperKEKB collides 7 GeV electrons against 4 GeV positrons, producing a centre-of-mass energy of $\sqrt{s} = 10.58\,\mathrm{GeV}$ that corresponds precisely to the mass of the $\Upsilon(4S)$ resonance. The $\Upsilon(4S)$ decays almost exclusively into pairs of B mesons ($\mathcal{B}[\Upsilon(4S) \to B\bar{B}] > 96\%$) [7], providing a clean environment in which to study B-meson decays without additional hadronic activity from the underlying event. The asymmetric beam energies give the $\Upsilon(4S)$ a Lorentz boost of $\beta\gamma \approx 0.28$ in the laboratory frame, displacing the two B-meson decay vertices along the beam axis by $\mathcal{O}(100\,\mu\mathrm{m})$ and thereby enabling time-dependent measurements of CP-violation asymmetries.

Belle II is the successor to the Belle detector and is designed to accumulate an integrated luminosity of $50\,\mathrm{ab}^{-1}$, approximately fifty times the full Belle dataset. The scientific programme encompasses precision measurements of B-meson and charm-hadron decays, searches for lepton-flavour-universality violation in semileptonic transitions $B \to D^{(*)}\ell\nu$, and broad sensitivity to physics beyond the Standard Model through rare and forbidden decay modes. Belle II's ability to reconstruct single charged-particle tracks with high momentum precision and to assign particle-species hypotheses through a multi-subsystem identification strategy is central to its diverse physics goals.

Belle II is a cylindrical, solenoidal detector placed around the SuperKEKB interaction point (IP). Moving radially outward from the beam axis, the detector consists of a pixel detector (PXD), a silicon vertex detector (SVD), a helium-based central drift chamber (CDC), two complementary Cherenkov-based particle-identification systems (TOP and ARICH), an electromagnetic calorimeter (ECL), a superconducting solenoid providing a 1.5 T axial field, and an outermost system for K_L^0 and muon identification (KLM).

Table 3.1 summarises all subsystems together with their channel counts and geometric acceptance.

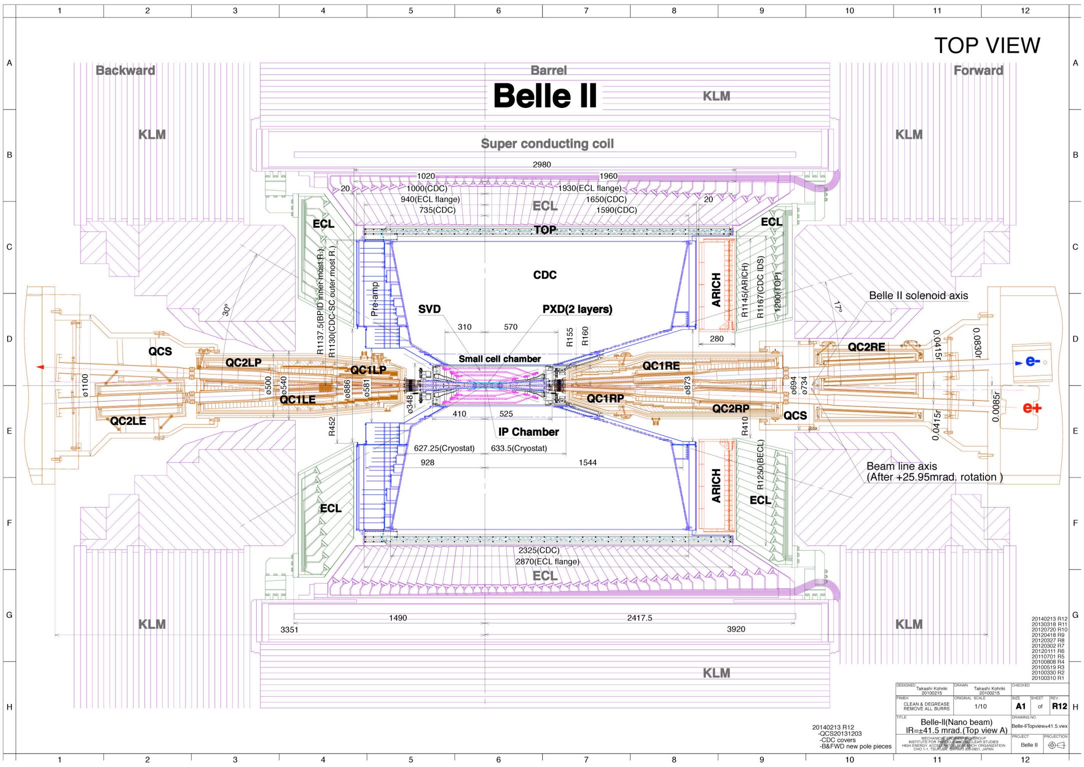

Figure 3.1: Top-view schematic of the Belle II detector showing all subsystems. The beam travels horizontally; the asymmetric beam energies produce a net boost toward the forward (right) direction. Figure from Ref. [4].

3.2 The Pixel and Silicon Vertex Detectors

The Pixel Detector (PXD) and the Silicon Vertex Detector (SVD) form the innermost tracking sub-systems and are central to any analysis requiring the reconstruction of secondary decay vertices. The inner region comprises two layers of pixel sensors (the PXD) and four outer layers of silicon strip sensors (the SVD).

3.2.1 Pixel Detector (PXD)

The PXD is based on Depleted Field Effect Transistor (DEPFET) pixel sensor technology, in which the readout transistor is integrated directly into the sensitive silicon bulk [4]. This monolithic design achieves a material budget of approximately 0.2% of a radiation length (X_0) per layer, roughly five times thinner than conventional hybrid pixel detectors, which is critical for minimising multiple Coulomb scattering and achieving the best possible impact-parameter resolution. The two PXD layers are located at mean radii

Table 3.1: Summary of Belle II detector subsystems. FWD and BWD denote forward and backward end-caps. Channel counts are approximate; refer to Ref. [4] for full details.

Purpose	**Component**	**Channels**	**θ coverage**	**R/z (mm)**
Tracking (PXD+SVD+CDC)	PXD	7.7×10^6	17°–150°	14–22
	SVD	245 k	17°–150°	38–140
	CDC	14 k	17°–150°	160–1130
Particle ID (PID)	TOP	8 k	31°–128°	∼1200
	ARICH	60 k	15°–35°	580–670
Calorimetry (ECL)	ECL Barrel	6624	32.2°–128.7°	1250–1620
	ECL FWD	1152	12.4°–31.4°	1962–2405
	ECL BWD	960	130.7°–155.1°	1022–1465
K_L^0+μ ID (KLM)	KLM Barrel	16 k / 41 k	40°–129°	2015–3320
	KLM End-caps	17 k	25°–40°, 129°–155°	,

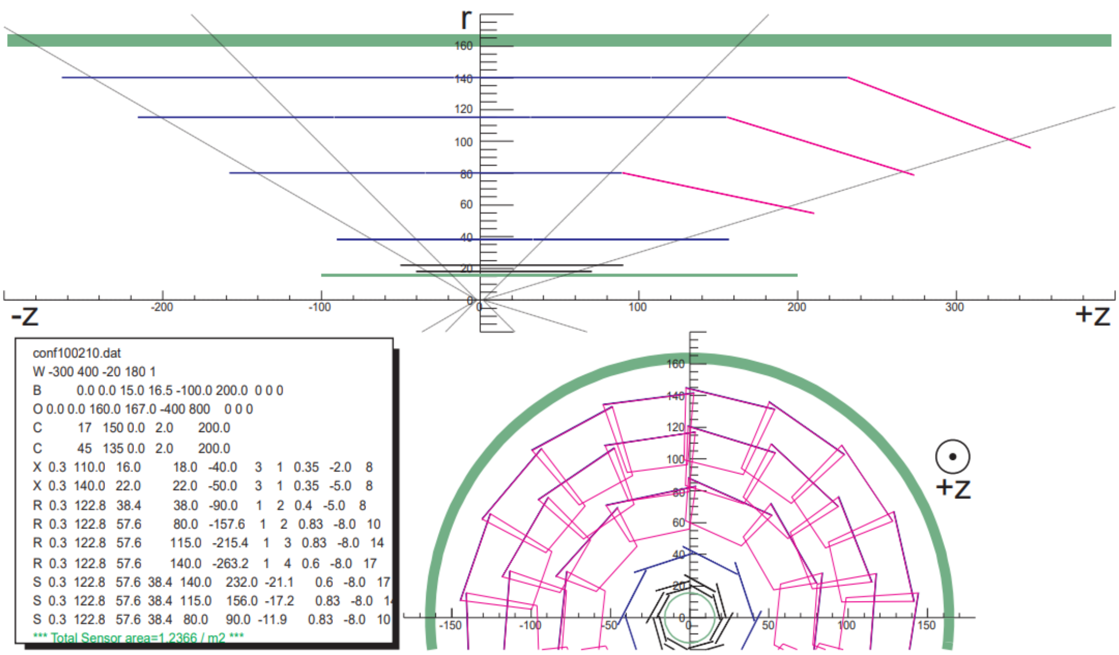

Figure 3.2: Cross-sectional view showing the two PXD layers (innermost) and the four SVD layers surrounding the beam pipe. Figure from Ref. [4].

of 14 mm and 22 mm from the IP, providing the closest possible position measurements to the primary collision point. With approximately 7.7×10^6 pixels in total, the PXD delivers hit-position resolutions of $\sim$10–20 μm in both the r-ϕ and z directions, enabling the reconstruction of B-meson decay vertices separated from the IP by only a few hundred micrometres.

The PXD, in combination with the SVD, plays a vital role in identifying displaced decay vertices. A precise determination of a track's transverse impact parameter d_0 and longitudinal impact parameter z_0 with respect to the IP is essential, both for vertex reconstruction and for background suppression against particles produced promptly at the IP.

3.2.2 Silicon Vertex Detector (SVD)

The SVD surrounds the PXD with four layers of double-sided silicon strip detectors (DSSDs) at radii between 38 mm and 140 mm, covering polar angles from 17° to 150° [4]. Each DSSD provides independent strip measurements on both the r-ϕ ("p-side") and z ("n-side") faces, giving full three-dimensional space points from a single detector layer. The 245 000 strips in total provide single-hit resolutions of approximately 10–30 μm, depending on the strip pitch and incidence angle. The SVD is the primary vertex-finding device for tracks with transverse momenta $p_T \gtrsim 50\,\mathrm{MeV}/c$, and its hits seed the global track reconstruction that combines PXD, SVD, and CDC information.

At low momenta (below $\sim$1 GeV/c), the SVD also contributes to particle identification via specific ionisation ($\mathrm{d}E/\mathrm{d}x$) in the silicon sensors, providing complementary proton–pion separation in a regime where the CDC ionisation measurement is less powerful.

3.3 The Central Drift Chamber

The Central Drift Chamber (CDC) is the primary tracking device of Belle II. It provides momentum measurements for all charged particles and a specific-ionisation signal used for hadron identification at low to intermediate momenta. The momentum and direction of charged particles are measured chiefly by the CDC, and its $\mathrm{d}E/\mathrm{d}x$ signal is the leading discriminant used to assign particle mass hypotheses to reconstructed tracks.

3.3.1 Design and Geometry

The CDC is a cylindrical wire chamber filled with a helium–ethane gas mixture ($\mathrm{He} : C_2H_6 = 50 : 50$ by volume) [4]. The use of helium as the primary carrier gas is deliberate: helium

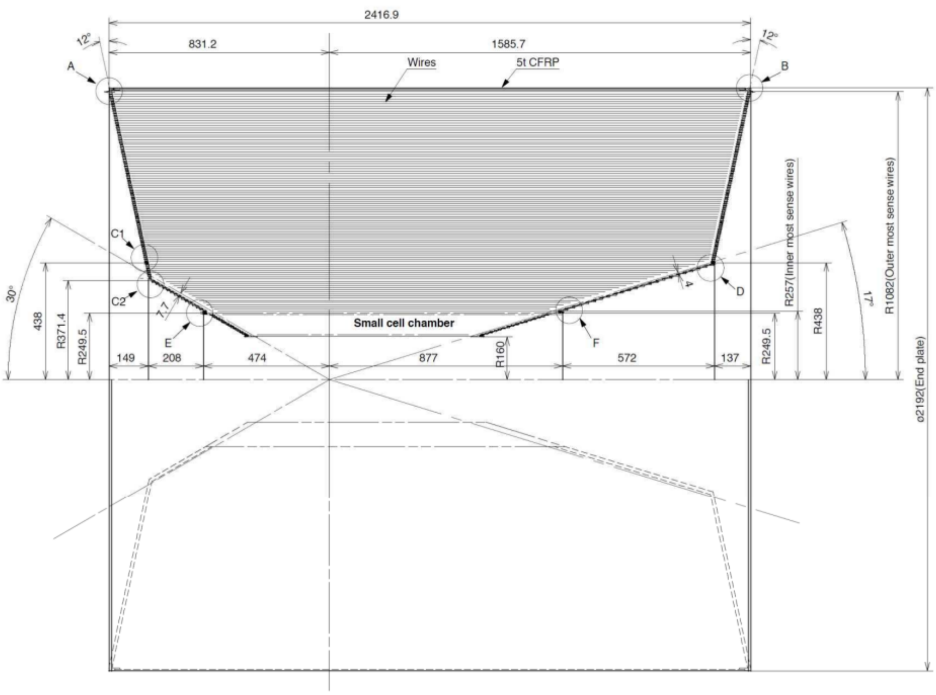

Figure 3.3: End-view cross-section of the Belle II Central Drift Chamber (CDC) showing the wire layout. Figure from Ref. [4].

has a radiation length approximately seven times larger than argon, reducing multiple Coulomb scattering within the chamber volume and thereby improving momentum resolution for low-momentum tracks. The active volume extends from an inner radius of 160 mm to an outer radius of 1130 mm, spanning 2350 mm along the beam axis, and covers polar angles from 17° to 150°, matching the inner tracker acceptance.

The CDC contains approximately 14 000 sense wires arranged in 56 layers, grouped into nine superlayers. The superlayers alternate between *axial* wire layers, running parallel to the beam axis and measuring the r-ϕ coordinates, and *stereo* wire layers, tilted by ±45–70 mrad relative to the axis to provide z-coordinate information. This architecture enables full three-dimensional track reconstruction without reliance on external z-reference devices. The single-cell hit resolution is approximately 100–130 μm in the drift direction, and the z resolution derived from the stereo superlayers is approximately 1–2 mm per superlayer.

3.3.2 Track Reconstruction and Momentum Resolution

Charged-particle tracks are reconstructed from the three-dimensional pattern of CDC hits combined with PXD and SVD space points in a global Kalman filter fit. The 1.5 T axial magnetic field, provided by the superconducting solenoid surrounding the CDC, causes charged particles to follow helical trajectories. A helix is parameterised by five quantities:

the signed transverse impact parameter d_0, the azimuthal angle at closest approach ϕ_0, the signed curvature $\kappa \equiv q/p_T$, the dip angle λ (complementary to the polar angle θ), and the longitudinal impact parameter z_0. The transverse momentum $p_T = q/(B\rho)$ is determined from the curvature of the helix in the magnetic field, and the full momentum vector follows from p_T and λ.

The combined tracking momentum resolution is parameterised as [4]

$$\frac{\sigma(p_T)}{p_T} \approx (0.2\% \cdot p_T\,[\mathrm{GeV}/c]) \oplus 0.3\%, \tag{3.1}$$

where $\oplus$ denotes addition in quadrature. The first term arises from the finite hit-position resolution and dominates at high momenta; the second arises from multiple Coulomb scattering and dominates at low momenta. For proton momenta in the range 0.3–2.8 GeV/c, the resolution transitions from the scattering-dominated to the measurement-dominated regime around 1.5 GeV/c.

The invariant mass of the B meson is reconstructed from four-momenta with appropriate mass hypotheses assigned, combined with the known $\Upsilon(4S)$ kinematics. Uncertainties in p_T and λ propagate directly into missing-mass kinematics, making the CDC momentum resolution a key systematic in missing energy measurements.

3.3.3 Specific Ionisation and Hadron Identification

In addition to its tracking function, the CDC measures the specific ionisation energy loss $\mathrm{d}E/\mathrm{d}x$ of charged particles as they traverse the gas volume. The charge deposited on each wire hit is recorded; after corrections for gain variations, path length, and Lorentz-angle effects, a truncated mean is formed from the lowest 80% of individual wire charge measurements to reduce the long tail of Landau fluctuations. The resulting estimator follows the Bethe–Bloch curve and provides a momentum-dependent particle-species discriminant.

The CDC $\mathrm{d}E/\mathrm{d}x$ resolution is approximately 5–6% for well-reconstructed tracks with many hit wires. This provides good separation between particle species where the Bethe–Bloch curves are well separated. For proton identification, the CDC $\mathrm{d}E/\mathrm{d}x$ is the primary discriminant below approximately 1 GeV/c, where protons are clearly distinguished from pions and kaons by their larger ionisation. Above ∼1 GeV/c, the curves converge in the relativistic rise region, and the Cherenkov-based PID systems (TOP and ARICH) take over as the dominant discriminators.

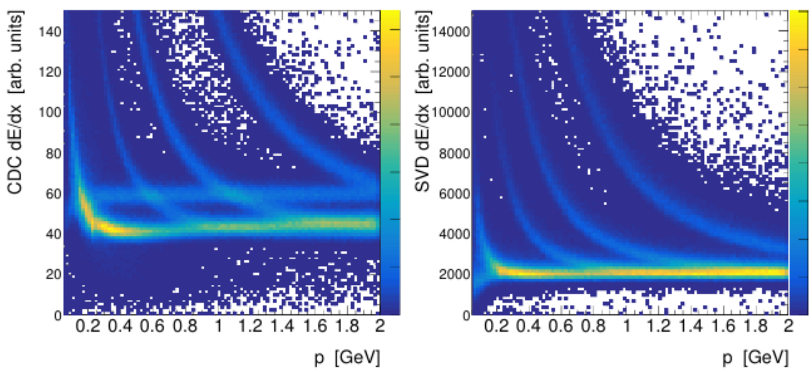

Figure 3.4: Specific ionisation dE/dx in the CDC (left) and in SVD (right) as a function of charged-particle momentum. The solid curves show the Bethe–Bloch expectation for each particle species. The proton band is clearly separated from pions and kaons below ∼1 GeV/c. Figure from Ref. [5].

3.4 Particle Identification Systems

Reliable assignment of particle-species hypotheses to reconstructed tracks is a prerequisite for invariant-mass reconstruction. Two dedicated Cherenkov-radiation detectors, the Time-Of-Propagation (TOP) counter in the barrel region and the Aerogel Ring-Imaging Cherenkov (ARICH) detector in the forward end-cap, complement the CDC dE/dx measurement and provide robust hadron identification across the full momentum range of interest.

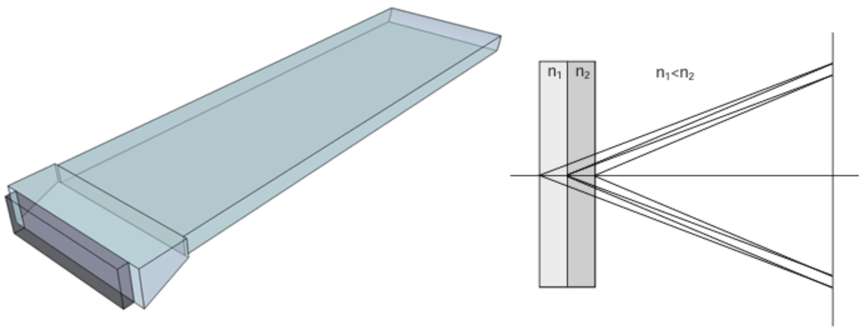

Figure 3.5: Belle-II PID systems: one of the modules of the TOP counter (left), principle of operation of the proximity focusing RICH with a non-homogeneous aerogel radiator in the focusing configuration (right). Figure from Ref. [5].

3.4.1 The Time-Of-Propagation Counter

The Time-Of-Propagation (TOP) counter occupies the barrel region between 31° and 128° in polar angle at a radius of approximately 1200 mm from the IP [4]. It consists of 16 azimuthal modules, each containing a 2.5 m long quartz bar that serves simultaneously as a Cherenkov radiator and as a light guide exploiting total internal reflection. A charged particle traversing the quartz emits Cherenkov photons at an angle

$$\cos\theta_C = \frac{1}{n\beta}, \tag{3.2}$$

determined by the particle's velocity β and the quartz refractive index $n \approx 1.473$. The Cherenkov photons propagate to the instrumented end of the bar, where an array of 512 MCP-PMTs (Micro-Channel Plate Photo-Multiplier Tubes) records the arrival time of each photon. The photon propagation time encodes both the Cherenkov angle θ_C (and hence the particle velocity) and the photon emission point along the bar.

The particle-identification signal is the probability distribution of photon arrival times, compared against the expected time pattern for each particle hypothesis $h \in \{e, \mu, \pi, K, p\}$ at the given track momentum. A likelihood $\mathcal{L}_{\mathrm{TOP}}(h)$ is computed for each hypothesis. The TOP achieves single-photon timing resolutions of approximately 100 ps, providing π/K separation at the $\geq 3\sigma$ level up to momenta of about 3.5 GeV/c, and useful proton–kaon separation up to $\sim$4 GeV/c [4].

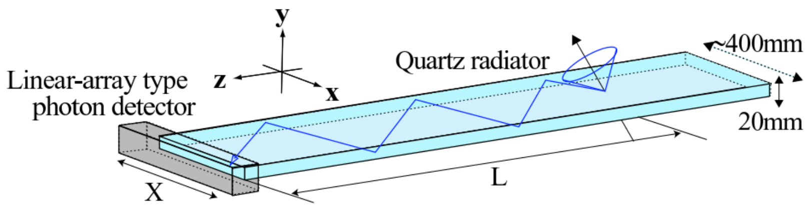

Figure 3.6: Schematic of a single TOP module showing the quartz bar, Cherenkov photon propagation by total internal reflection. Figure from Ref. [4].

3.4.2 The ARICH Detector

The Aerogel Ring-Imaging Cherenkov (ARICH) detector covers the forward end-cap region from 15° to 35° in polar angle, where the asymmetric beam conditions produce the highest-momentum forward-going tracks [4]. It consists of two focusing aerogel layers with refractive indices $n_1 \approx 1.045$ and $n_2 \approx 1.055$, chosen so that the Cherenkov rings from the two layers constructively overlap on the photon-detection plane located $\sim$20 cm downstream. The photons are detected by approximately 60 000 channels of Hybrid Avalanche Photo Detectors (HAPDs), which are radiation-hard devices capable of operating in the 1.5 T magnetic field.

The ring-imaging geometry provides a direct measurement of the Cherenkov angle θ_C and hence of the particle velocity β. Combined with the momentum p measured by the

CDC, this yields the particle mass $m = p\sqrt{1-\beta^2}/\beta$. The ARICH achieves a Cherenkov-angle resolution of $\sim$14 mrad per track, providing π/K separation at the $\geq 3\sigma$ level up to momenta of about 3.5 GeV/c in the forward region [4]. Proton identification also benefits from the ARICH, complementing the CDC dE/dx measurement for forward tracks outside the TOP acceptance.

3.4.3 Combined PID Likelihood and Proton Performance

The outputs of the CDC dE/dx measurement, the TOP timing likelihood, and the ARICH ring-imaging likelihood are combined into a global particle-identification likelihood for each track. For a given particle hypothesis h, the combined log-likelihood is

$$\ln \mathcal{L}(h) = \ln \mathcal{L}_{\mathrm{CDC}}(h) + \ln \mathcal{L}_{\mathrm{TOP}}(h) + \ln \mathcal{L}_{\mathrm{ARICH}}(h), \tag{3.3}$$

where independence of the sub-detector measurements is assumed. A binary log-likelihood ratio (LLR) between a given hypothesis and the next most probable hypothesis typically forms the basis of particle selection criteria.

Belle II has not yet published a comprehensive proton identification efficiency measurement covering the full momentum range. The expected performance is benchmarked against the BABAR detector, which employed an analogous Cherenkov sub-system (the DIRC). BABAR reports a pion fake rate below 2% for proton identification efficiencies of 90% or higher across the momentum range relevant to B-meson decay studies [8]. The Belle II combined PID system, with the additional ARICH coverage in the forward region and the improved single-photon timing resolution of the TOP relative to BABAR's DIRC, is expected to match or exceed this benchmark.

3.5 Other Detector Components

Beyond the tracking and particle-identification sub-systems described above, Belle II includes an electromagnetic calorimeter (ECL) and a K^0_L-and-muon identification system (KLM). These components contribute to event-level background suppression and play an important role in the broader Belle II physics programme. They are summarised briefly here for completeness.

3.5.1 Electromagnetic Calorimeter (ECL)

The electromagnetic calorimeter measures photon and electron energies through electromagnetic showering in thallium-doped caesium iodide CsI(Tl) crystals [4]. The ECL consists of 8 736 crystals arranged in a barrel (6 624 crystals, 32.2°–128.7°) and two end-caps: a forward end-cap with 1 152 crystals (12.4°–31.4°) and a backward end-cap with 960 crystals (130.7°–155.1°). The energy resolution achieved is approximately

$$\frac{\sigma(E)}{E} \approx \frac{1.34\%}{E^{1/4}\,[\mathrm{GeV}^{1/4}]} \oplus 0.11\% \oplus \frac{1.57\%}{E\,[\mathrm{GeV}]}, \tag{3.4}$$

from simulation [4]. The ECL is the primary device for reconstructing neutral particles (π^0, η, γ) and for electron identification via the ratio of deposited energy to CDC momentum E/p. The ECL is often used to veto events containing energetic photons and contributes to the computation of the total visible four-momentum used to infer missing-mass kinematics.

3.5.2 The K_L^0 and Muon Identification System (KLM)

The KLM is the outermost active sub-system of Belle II, located outside the superconducting solenoid between radii of 2015 mm and 3320 mm in the barrel, and covering the forward (25°–40°) and backward (129°–155°) end-cap regions [4]. It alternates 4.7 cm thick iron absorber plates, which also return the solenoid magnetic flux, with active detector layers. In the barrel, the active elements are resistive plate chambers (RPCs, ∼16 k channels) supplemented by scintillator-based layers (∼41 k channels) to cope with higher background rates near the beam axis; the end-caps use scintillator strips exclusively (∼17 k channels).

Muons are identified by requiring a charged track to penetrate multiple iron absorber layers with a hit pattern consistent with a minimum-ionising particle. Pions and kaons undergo hadronic interactions in the iron and are typically absorbed before reaching the outer KLM layers, providing good muon purity. K_L^0 mesons are detected through the hadronic shower they initiate in the absorber iron, which produces a cluster of KLM hits that can be reconstructed as a neutral KLM object with directional information.

The KLM is heavily used in event-level vetos of muon-rich backgrounds, in particular, to suppress semileptonic B decays involving a muon that could be misidentified as a hadron. Muon vetos based on KLM hit patterns are therefore applied as part of event selection, complementing the PID likelihood selection.

In summary, Belle II provides an integrated suite of subdetectors that enable the full reconstruction of B-meson decays. The PXD and SVD provide precise decay-vertex measurements, while the CDC measures charged-particle momenta and supplies the dominant particle-identification input at low momenta. The TOP and ARICH systems extend hadron identification to intermediate and high momenta. The electromagnetic calorimeter (ECL) is primarily used for the detection and energy measurement of photons and electrons, while the K-long and muon detector (KLM) is responsible for identifying muons and detecting long-lived neutral hadrons such as KL0. Together, these systems also play an important role in event-level background suppression. The combined performance of the detector, particularly the track momentum resolution, vertex impact-parameter resolution, and particle-identification efficiency, directly determines the sensitivity of the experiment's diverse physics programme.

Chapter 4

Experimental Signature and Search Strategies

The combination of rare production and long-lived decays leads to a distinctive experimental signature: a displaced vertex (DV) with multiple charged tracks originating away from the primary interaction point. Such multi-track displaced vertices are relatively rare in Standard Model processes, making them experimentally clean probes of new physics. However, residual backgrounds from long-lived Standard Model hadrons and detector effects necessitate careful background estimation and suppression strategies. Experiments such as Belle II are particularly well suited for these searches due to their high luminosity and excellent vertex reconstruction capabilities. The precise tracking system enables accurate reconstruction of displaced decay points and associated charged-particle multiplicities.

In this chapter, we discuss search strategies for long-lived neutralino decays, focusing on both exclusive channel-based approaches and inclusive methods targeting generic multi-track displaced vertices.

4.1 Exclusive Search Strategy

Overview of the Exclusive Approach

The exclusive search strategy focuses on the full reconstruction of specific, predefined neutralino decay chains. In this approach, the signal is defined by the primary production mechanism,

$$B^+ \to p\,\tilde{\chi}_1^0, \tag{4.1}$$

followed by the decay of the neutralino into specific hadronic final states, such as

$$\tilde{\chi}_1^0 \to \Lambda_c K, \quad \Sigma_c K_S^0, \quad \text{or} \quad \Xi_c \pi. \tag{4.2}$$

To fully reconstruct these final states, the analysis relies on identifying the dominant decay modes of the intermediate charmed baryons (e.g., $\Lambda_c^+ \to pK^-\pi^+$, $\Sigma_c \to \Lambda_c\pi$, or $\Xi_c \to \Xi\pi\pi \to \Lambda\pi\pi\pi$). By ensuring every final-state particle is accounted for, this strategy produces fully reconstructible event topologies with highly constrained kinematics.

Hierarchical Reconstruction and Kinematic Identification

The exclusive reconstruction proceeds hierarchically from the bottom up. First, stable charged tracks are selected, applying rigorous particle identification (PID) requirements to accurately distinguish between protons, kaons, and pions. These tracks are then used to reconstruct long-lived intermediate states, such as K_S^0, Λ, and Ξ, using vertex fitting and invariant mass windows to improve resolution and reject background.

Following this, charmed baryons (Λ_c, Σ_c, Ξ_c) are reconstructed from their respective decay products. The neutralino candidate is subsequently formed by combining the reconstructed charmed baryon with an additional meson (K, K_S^0, or π). Finally, the B^+ candidate is reconstructed by combining the neutralino candidate with the prompt proton from the primary vertex.

At the top of the decay chain, the identification of the signal B meson relies on two standard kinematic variables used extensively in Belle II analyses: the beam-constrained mass, M_{bc}, and the energy difference, ΔE. These are defined as:

$$M_{\text{bc}} = \sqrt{E_{\text{beam}}^2 - |\vec{p}_B|^2}, \tag{4.3}$$

$$\Delta E = E_B - E_{\text{beam}}, \tag{4.4}$$

where E_{beam} is the beam energy, and $(E_B, \vec{p}_B)$ is the four-momentum of the reconstructed B meson in the center-of-mass frame. Signal candidates are characterized by M_{bc} peaking at the nominal B meson mass and ΔE around zero.

Background Suppression: Displaced Vertices and Event Shape

A defining feature of the signal is the macroscopic lifetime of the neutralino, which yields a displaced decay vertex (DV). The exclusive analysis exploits this topology by imposing stringent displacement requirements on the reconstructed neutralino vertex. In particular, a requirement on the transverse displacement is applied:

$$d_r(\tilde{\chi}_1^0) > 1\,\text{cm}. \tag{4.5}$$

These requirements effectively eliminate prompt Standard Model backgrounds, which predominantly originate near the interaction point.

In addition, continuum background from ($e^+e^- \to q\bar{q}$) processes is reduced using event-shape variables, which help distinguish the more spherical signal topology from the jet-like structure of continuum events. The implementation of these event-shape-based suppression techniques is being carried out by other groups within the Belle IIcollaboration.

Strengths and Challenges of the Exclusive Approach

The primary strength of the exclusive strategy lies in its exceptional background suppression. By requiring the full reconstruction of a specific decay chain and applying tight invariant mass constraints at every intermediate step, the analysis achieves a highly pure signal region in the M_{bc}–ΔE plane.

However, fully reconstructing all final-state particles introduces several inherent challenges. Since the method targets only a predetermined subset of possible neutralino decay channels, it provides limited coverage of the total signal phase space. Furthermore, the overall signal efficiency is significantly reduced due to the cumulative inefficiencies of tracking and PID for multi-body final states; a single missed or misidentified track prevents the reconstruction of the entire event. Finally, the analysis relies heavily on theoretical assumptions regarding the dominant decay modes and branching fractions of the neutralino.

These challenges highlight the strong complementarity of an inclusive search strategy. By relaxing the requirement to fully reconstruct intermediate hadronic states, an inclusive approach can retain sensitivity to a wider range of neutralino decays, recovering events that would otherwise be lost due to reconstruction inefficiencies or decay modes not explicitly targeted.

4.2 Inclusive Search Strategy

Concept of the Inclusive Approach

Unlike the exclusive strategy, which reconstructs specific decay chains of the neutralino, the inclusive search aims to identify signal events without requiring full reconstruction of the final state.

In this approach, the signal is defined by the process

$$B^+ \to p\,\tilde{\chi}_1^0, \tag{4.6}$$

where the neutralino subsequently decays into a displaced vertex (DV) with multiple charged tracks:

$$\tilde{\chi}_1^0 \to \mathrm{DV} + \text{anything}. \tag{4.7}$$

Only partial information is used:

- the prompt proton from the B decay,
- the position of the displaced vertex,
- the charged tracks associated with the DV.

No assumption is made about the specific hadronic decay mode of the neutralino. This allows the analysis to remain sensitive to a broad class of final states, including all decays producing at least four charged tracks.

Kinematic Observables and Constraints

The inclusive method exploits kinematic constraints from the decay chain

$$B^+ \to p\,\tilde{\chi}_1^0, \quad \tilde{\chi}_1^0 \to \mathrm{DV} + \text{any}. \tag{4.8}$$

The following quantities are experimentally measured:

- four-momentum of the proton p_p^μ,
- position vector of the displaced vertex $\vec{r}_{\mathrm{DV}}$,
- center-of-mass energy $\sqrt{s}$.

The unknown quantities include:

- neutralino four-momentum,
- momentum of the unobserved final-state particles,
- B meson four-momentum.

These unknowns are constrained by:

- four-momentum conservation at the B decay vertex,
- four-momentum conservation at the neutralino decay,
- alignment of the neutralino momentum with the DV direction,
- known B meson mass,
- beam energy constraint in the center-of-mass frame.

Altogether, these provide a system of equations sufficient to reconstruct the neutralino kinematics up to a discrete ambiguity.

Mass Reconstruction

Here's an explicit calculation for the neutralino mass using the kinematic constraints described above. Constraints are:

- four-momentum conservation at the B^+ decay,
- the beam-energy constraint in the center-of-mass (CM) frame,
- the geometrical alignment of the neutralino momentum with the displaced vertex.

Step 1: Neutralino energy in the CM frame In the center-of-mass frame of the e^+e^- collision, the B meson energy is fixed:

$$E_B^* = \frac{\sqrt{s}}{2}. \tag{4.9}$$

Using four-momentum conservation for $B^+ \to p\,\tilde{\chi}_1^0$,

$$p_B^\mu = p_p^\mu + p_\chi^\mu, \tag{4.10}$$

the neutralino energy is

$$E_\chi^* = E_B^* - E_p^*. \tag{4.11}$$

Step 2: Directional constraint The displaced vertex provides the direction of the neutralino momentum:

$$\vec{p}_\chi = p_\chi\,\hat{n}, \qquad \hat{n} = \frac{\vec{r}_{\rm DV}}{|\vec{r}_{\rm DV}|}. \tag{4.12}$$

We define

$$c_\chi \equiv \cos\theta_\chi = \hat{n}\cdot\hat{z}, \qquad c_{p\chi} \equiv \cos\theta_{p\chi} = \hat{p}_p\cdot\hat{n}. \tag{4.13}$$

Step 3: Boost to the laboratory frame At Belle II, the CM frame is boosted along the z-axis. Denoting the boost parameters by β and γ, the neutralino energy transforms as

$$E_\chi = \gamma \left(E_\chi^* + \beta \, p_\chi^* c_\chi \right) . \tag{4.14}$$

Similarly, the proton quantities in the CM and lab frames are related by the same boost.

Step 4: Solve for the neutralino momentum Using the invariant mass condition for the B meson,

$$m_B^2 = (p_p + p_\chi)^2, \tag{4.15}$$

and writing $p_\chi = p_\chi \hat{n}$, one obtains a quadratic equation in p_χ. After algebraic simplification, this can be written as

$$A \, p_\chi^2 + B \, p_\chi + C = 0, \tag{4.16}$$

where

$$A = 1 - \beta^2 c_\chi^2, \tag{4.17}$$

$$B = -2 \left(p_p c_{p\chi} - \beta^2 p_p^z c_\chi - \frac{E_B}{\gamma} \beta c_\chi \right) , \tag{4.18}$$

$$C = M_B^2 + p_p^2 - \beta^2 (p_p^z)^2 - 2 \frac{E_B}{\gamma} \beta p_p^z. \tag{4.19}$$

The solution is therefore

$$p_\chi = \frac{-B \pm \sqrt{B^2 - 4AC}}{2A}. \tag{4.20}$$

Step 5: Neutralino mass reconstruction Once p_χ is determined, the neutralino mass follows from the energy-momentum relation:

$$m_{\tilde{\chi}_1^0}^2 = E_\chi^2 - p_\chi^2. \tag{4.21}$$

Discrete ambiguity Due to the quadratic nature of the solution for p_χ, each event yields two possible solutions:

$$m_{\tilde{\chi}_1^0}^2 \;\to\; (m_+, \, m_-). \tag{4.22}$$

This two-fold ambiguity reflects the incomplete reconstruction arising from the unobserved particles in the neutralino decay.

Properties of the Kinematic Solutions

The (m_+, m_-) solutions provide a powerful discriminant between signal and background:

- Signal events tend to cluster around the true neutralino mass in the (m_+, m_-) plane.
- Background events populate a broader region and do not exhibit such a correlation.

For a given neutralino mass hypothesis, selecting events within an appropriate region of the (m_+, m_-) plane can retain a large fraction of signal while rejecting a significant portion of background.

It is important to note that for a fraction of events, no physical solution exists due to detector resolution effects or imperfect reconstruction.

Advantages of the Inclusive Strategy

The inclusive approach offers several advantages over the exclusive reconstruction:

- **Broad signal acceptance:** Sensitive to all neutralino decay modes with sufficient charged track multiplicity.
- **Higher efficiency:** Does not require full reconstruction of intermediate states.
- **Improved sensitivity:** Expected to provide significantly better reach compared to exclusive searches, provided backgrounds are controlled.

However, this approach comes with increased challenges in background modelling and control, particularly from material interactions and combinatorial sources.

Chapter 5

Data Sample Generation

In this analysis, the primary signal scenario involves a light, long-lived neutralino ($\tilde{\chi}^0$) that decays via baryonic R-parity violating (RPV) couplings into three quarks (e.g., u, d, s). Because quarks carry color charge, they cannot be observed freely due to color confinement; instead, they must hadronize to produce the detector-visible particles we reconstruct in the Belle II detector. Hadronization is the non-perturbative transition phase whereby free partons are bound into color-singlet hadrons. Alternatively referred to as fragmentation, this process cannot be computed from first principles in perturbative Quantum Chromodynamics (pQCD) and is therefore generally simulated or analyzed using phenomenological models. The two most prominent models in high-energy physics are the Lund string fragmentation model (implemented in Pythia8) and the cluster hadronization model (implemented in Herwig7).

Because our search is meant to be highly inclusive and robust against theoretical uncertainties, we aim to include multiple hadronization models to evaluate systematic variations. In this chapter, both models are explained in rigorous detail, along with a description of our methodology for generating the signal samples.

Furthermore, we include signal samples generated directly from exclusive form factor calculations, specifically derived for B-meson decays as presented in recent theoretical frameworks [1]. While inclusive hadronization models are highly effective at large invariant masses, light neutralinos ($1 \lesssim m_{\tilde{\chi}^0} \lesssim 3$ GeV/c^2) predominantly decay into few-body final states. By incorporating both the high-multiplicity final states via standard hadronization models and the more constrained, likely dominant, exclusive baryon-meson pairs via form factors, we create a robust testing ground. This approach allows us to critically evaluate our signal extraction and background rejection algorithms across the full phase space, significantly solidifying the analysis.

5.1 Form Factor Calculation for Exclusive Decays

For GeV-scale neutralinos, the available phase space for the decay $\tilde{\chi}_1^0 \to q_i q_j q_k$ is strongly constrained. In this regime, the assumption of inclusive quark production followed by independent fragmentation becomes unreliable, as hadronization is dominated by low-lying exclusive states. Consequently, the decay must be described in terms of exclusive baryon–meson final states using hadronic transition form factors.

In baryonic R-parity violating (RPV) supersymmetry, the relevant interaction arises from the $\lambda''_{ijk} U_i^c D_j^c D_k^c$ operators. After integrating out the heavy squark mediators, one obtains an effective four-fermion interaction that couples the neutralino to three quarks. At low energies, these quark-level operators are matched onto hadronic degrees of freedom using an $SU(3)$-flavor phenomenological Lagrangian describing baryon multiplets.

In this framework, the dominant decay modes of the neutralino are exclusive two-body processes of the form

$$\tilde{\chi}_1^0 \to \mathcal{B} + \mathcal{M}, \tag{5.1}$$

where $\mathcal{B}$ denotes a baryon (e.g. p, Λ, Σ, or charmed baryons such as Λ_c) and $\mathcal{M}$ denotes a pseudoscalar meson (e.g. π, K). The corresponding hadronic matrix elements are parameterized in terms of transition form factors derived within the $SU(3)$ effective theory and supplemented by phenomenological inputs.

The transition amplitude for such processes is expressed as

$$\mathcal{M} \propto \langle \mathcal{B}(p_{\mathcal{B}})\, \mathcal{M}(p_{\mathcal{M}}) | \mathcal{O}_{UDD} | 0 \rangle, \tag{5.2}$$

where the non-perturbative QCD dynamics are fully encoded in the baryon–meson form factors. These form factors are computed using the phenomenological Lagrangian approach and explicitly tabulated for the relevant channels (see Appendix A of the reference [1]).

The decay width for a two-body channel is then given by

$$\Gamma(\tilde{\chi}_1^0 \to \mathcal{B}\mathcal{M}) = \frac{|\vec{p}_{\mathcal{B}}|}{8\pi m_{\tilde{\chi}_1^0}^2} |\mathcal{M}|^2, \tag{5.3}$$

with $|\vec{p}_{\mathcal{B}}|$ evaluated in the neutralino rest frame.

This exclusive treatment leads to sharply defined final-state kinematics, characterized by a baryon recoiling against a meson with fixed momentum. Such topologies are essential for accurately modeling displaced-vertex signatures and are directly implemented in the Monte Carlo simulations used to estimate Belle II sensitivities.

5.2 Pythia8: The Lund String Fragmentation

For neutralinos with larger masses, multi-body final states become accessible, and the decay is more appropriately modeled inclusively using the Lund String Fragmentation model as implemented in PYTHIA8.

The Lund model is grounded in the phenomenological observation of linear confinement in QCD. As a quark (q) and an antiquark ($\bar{q}$) move apart following a hard interaction, the color flux between them is constrained to a narrow tube or "string" due to the self-interacting nature of gluons. This color string has an approximately constant energy density (string tension), typically denoted as $\kappa \approx 1$ GeV/fm (~ 0.2 GeV^2). The potential energy stored in the string increases linearly with the distance separating the partons, $V(r) = \kappa r$.

As the quarks separate, the potential energy eventually exceeds the threshold necessary to create a new quark-antiquark pair ($q'\bar{q}'$) from the vacuum. The string then "breaks", producing two new color-singlet systems: a $q\bar{q}'$ and a $q'\bar{q}$. This process is governed by a quantum mechanical tunneling mechanism analogous to the Schwinger effect in QED. The probability of creating a pair with transverse mass $m_\perp = \sqrt{m^2 + p_\perp^2}$ is given by:

$$\mathcal{P} \propto \exp\left(-\frac{\pi m_\perp^2}{\kappa}\right) = \exp\left(-\frac{\pi m^2}{\kappa}\right) \exp\left(-\frac{\pi p_\perp^2}{\kappa}\right). \tag{5.4}$$

This exponential suppression naturally explains why the production of heavy quarks (s, c, b) is strongly penalized during fragmentation compared to light quarks (u, d), and it naturally generates the transverse momentum distribution of the resulting hadrons.

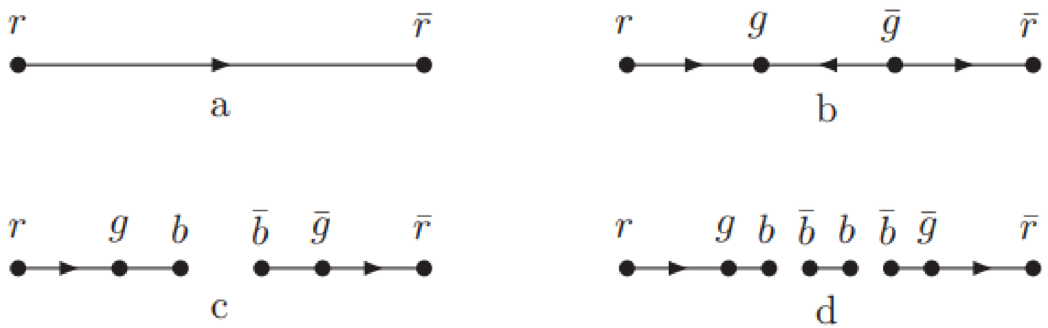

Figure 5.1: Illustration of step-wise popcorn production of a baryon–antibaryon pair with a meson in between. In (a), a string is formed between an $r\bar{r}$ quark–antiquark pair, with the colour flow indicated by arrows. In (b), a $g\bar{g}$ quark–antiquark pair is produced as a vacuum fluctuation, reversing the colour flow in the central region. In (c), another pair is produced, breaking the string, and in (d), a further breakup produces a meson between the baryon and antibaryon. Figure from Ref. [9].

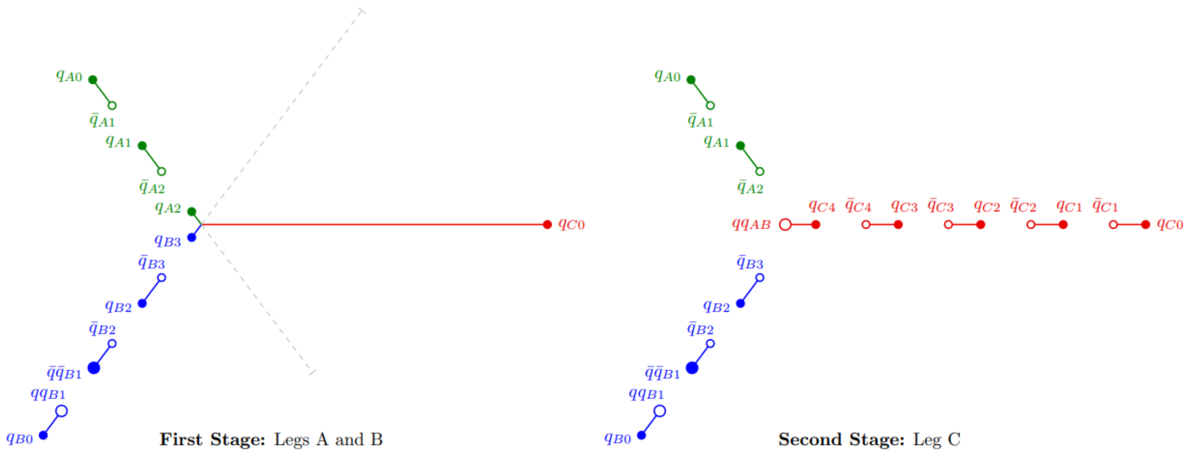

Figure 5.2: Illustration of the two stages of junction fragmentation. In the first stage (left), the junction rest frame (JRF) is defined such that the three legs are separated by 120°; if no solution is found, the center-of-mass frame is used. The two lowest-energy legs (A and B) are then fragmented inwards from their endpoints, stopping when further hadrons would have negative rapidity. In the second stage (right), the remaining quark endpoints are combined into a diquark (qq_{AB}), which serves as an endpoint for the final string. This string is then fragmented in the standard way, alternating between the two endpoints.

The fragmentation process is iterative. A meson is ”peeled off” from the end of the string, leaving a remainder string with reduced energy. The fraction of the string's longitudinal momentum (z) carried away by the newly formed hadron is determined by the Lund symmetric fragmentation function:

$$f(z) = \frac{N}{z}(1-z)^a \exp\left(-\frac{bm_\perp^2}{z}\right), \tag{5.5}$$

where a and b are phenomenological parameters tuned to experimental data, and N is a normalization constant.

5.2.1 Junction Fragmentation for Baryonic RPV

In the specific context of baryonic R-parity violation ($\tilde{\chi}^0 \to q_i q_j q_k$), the decaying particle produces three quarks and no antiquarks, carrying a net baryon number of 1. In color space, three quarks form a color singlet by tying together in a Y-shaped topology, meeting at a central point called a *color junction*.

Pythia8 utilizes a dedicated junction fragmentation mechanism to handle this scenario, as shown in the figure. Each of the three quarks is attached to a string that terminates at the central junction. As the quarks move outward, the strings break independently, producing mesons. Eventually, the three remainder strings become short enough that the three innermost partons (closest to the junction) combine to form the final baryon. This topological approach correctly conserves baryon number and generates the high-multiplicity hadronic environments we anticipate for heavier neutralino masses.

5.3 Herwig: Cluster Hadronization

As an alternative systematic probe, we utilize HERWIG7, which employs the Cluster Hadronization model. While the string model relies heavily on a top-down phenomenological approach to confinement, the cluster model is built from the bottom up, relying heavily on the principle of *preconfinement* inherent in perturbative QCD.

According to preconfinement, the color structure of the partons at the end of a perturbative parton shower naturally arranges them into localized, color-singlet configurations whose mass distributions are asymptotically independent of the hard scattering energy scale. HERWIG models this by forcing all final-state gluons from the parton shower to non-perturbatively split into $q\bar{q}$ pairs.

Following this splitting, adjacent quarks and antiquarks in color space are paired to form color-singlet entities called *clusters*. These clusters can be thought of as highly excited, continuous hadronic resonances. The mass spectrum of these primary clusters peaks at relatively low masses (typically a few GeV/c^2) and falls off rapidly.

If a primary cluster is excessively massive, above a tunable threshold, typically denoted as M_{max} or `ClMaxLight`, it undergoes *cluster fission*. The heavy cluster splits along the string-like direction of its constituent partons into two lighter clusters. This fission process continues iteratively until the resulting clusters fall below the mass threshold.

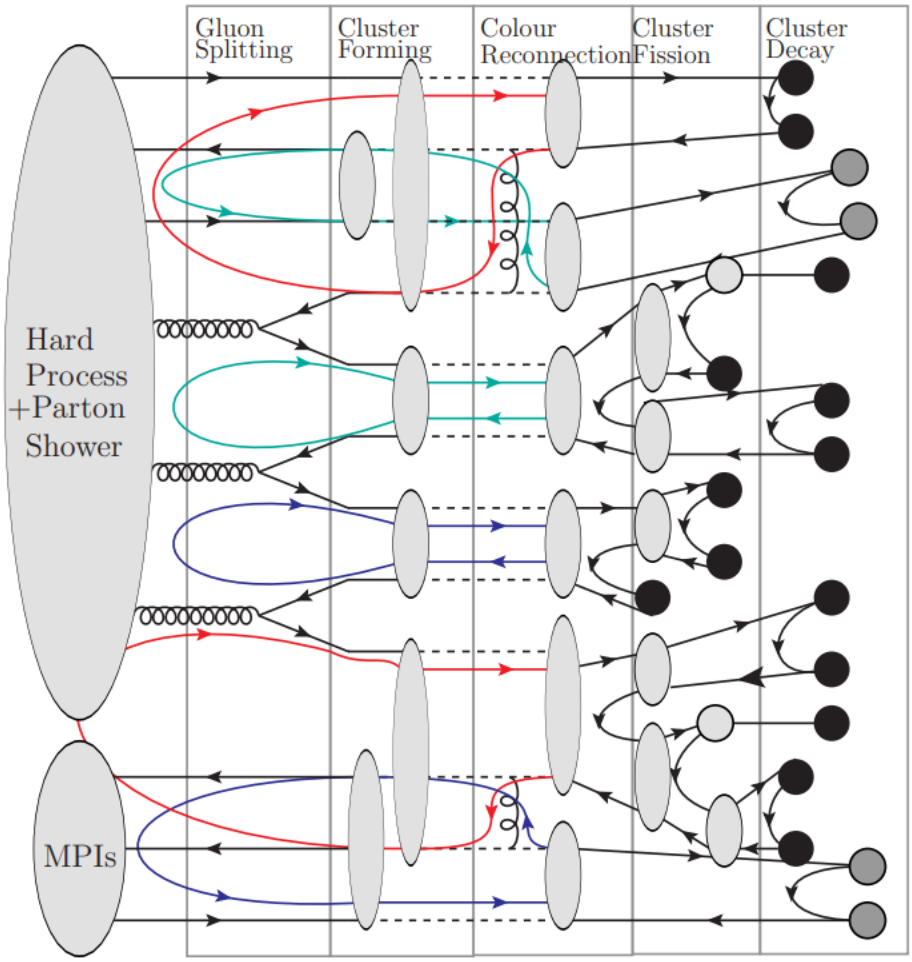

Figure 5.3: Schematic representation of the Cluster Hadronization model used in HERWIG7. Gluons undergo non-perturbative splitting into quark-antiquark pairs, which are then grouped by color flow into singlet clusters before decaying into observable hadrons.

Once the clusters are sufficiently light, they decay isotropically in their respective rest frames into pairs of primary hadrons. The branching ratio for a cluster of mass M_c to decay into two hadrons h_1 and h_2 with masses m_1 and m_2 and spins S_1 and S_2 is governed strictly by the phase space and spin degeneracy:

$$\Gamma(C \to h_1 h_2) \propto (2S_1 + 1)(2S_2 + 1)P^*(M_c, m_1, m_2), \tag{5.6}$$

where P^* is the center-of-mass momentum of the decay products.

Because cluster hadronization relies purely on phase space and spin degeneracy for the final hadron selection, it makes fundamentally different predictions compared to the Lund string model regarding strangeness suppression, baryon production rates, and transverse momentum distributions. By incorporating samples generated with HERWIG7, we aim to introduce a conservative, robust envelope for modeling the systematic uncertainty stemming from non-perturbative QCD effects, this sample generation is in progress.

5.4 General Workflow for Signal Generation

In Belle II, the simulation software framework, `basf2` (Belle II Analysis Software Framework), orchestrates the flow of event generation, simulation, and reconstruction. For this analysis, ensuring correct signal decay kinematics and lifetimes requires a tightly coordinated generator chain.

The initial electron-positron collision and the production of the $\Upsilon(4S)$ resonance are handled first. The decay of the B-mesons into our hypothetical long-lived neutralino is primarily managed by EvtGen. To facilitate this, we construct custom `DEC` (decay) files. EvtGen is uniquely powerful in modeling heavy flavor decays because it correctly propagates the spin-density matrices through the decay chain, preserving angular correlations.

For the different modeling approaches, the `DEC` files instruct `basf2` differently:

- **Form Factor Model:** In the exclusive case, the `DEC` file defines the neutralino as a long-lived particle and explicitly lists the branching fractions for baryon-meson pair. EvtGen utilizes a customized phase-space or form-factor-driven amplitude model (branching fractions) to decay the neutralino at its displaced vertex.

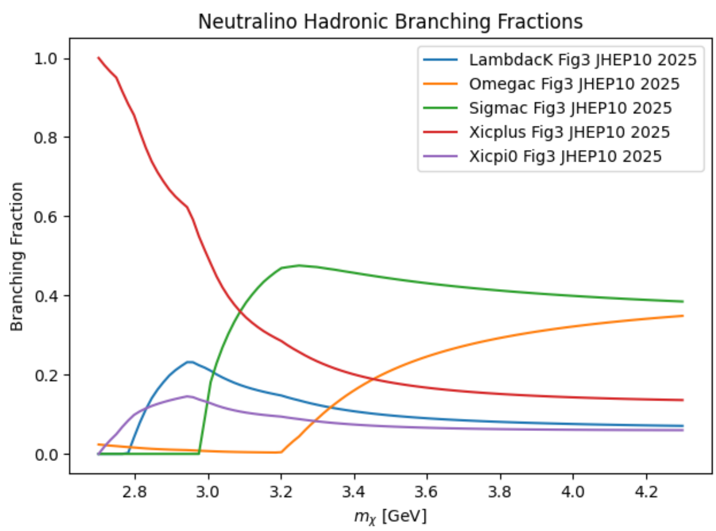

Figure 5.4: Branching fractions calculated using form factor, individual widths and total width are taken from the fig.3 and fig.4 of [1]

- **Inclusive String/Cluster Models:** In the inclusive approach, `Pythia8` is used to decay the neutralino into three constituent quarks (e.g., u, d, s). These partons are then hadronized using the string/cluster hadronization model implemented in `Pythia8`/Herwig7, yielding primary baryon–meson pairs along with their corresponding branching fractions. This procedure is performed for neutralino masses in the range 2.7–4.3 GeV. The resulting decay information is used to construct custom

DEC files, which are subsequently provided to basf2 (via EvtGen) to simulate the decay and generate the final-state particles.

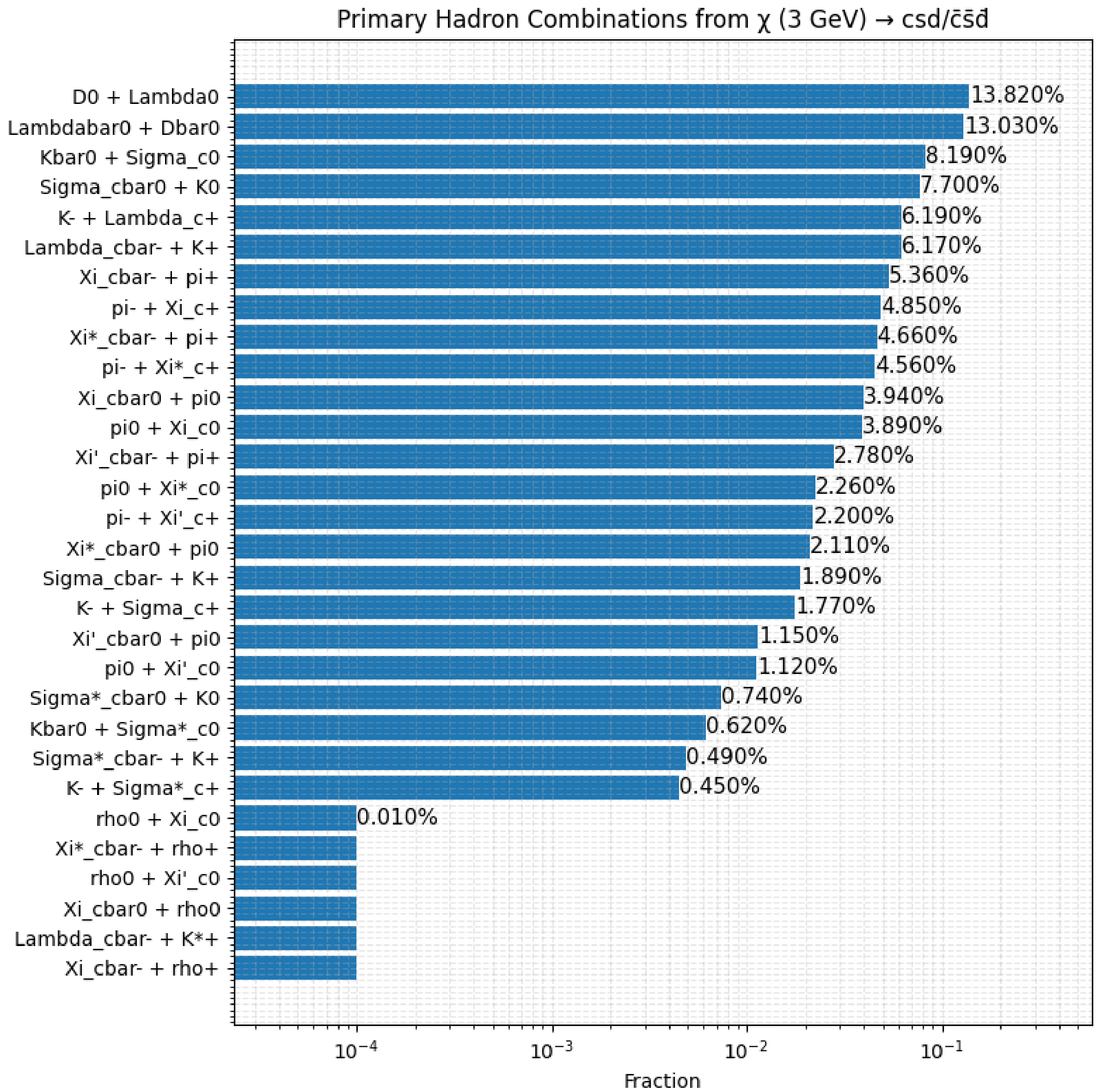

Figure 5.5: Branching fractions calculated using pythia8 hadronization model

A critical aspect of signal generation is the long lifetime of the neutralino ($c\tau$). The displacement of the decay vertex must be properly simulated in the detector geometry. basf2 passes the generated particles into a full Geant4-based detector simulation. The decay products of the neutralino originating far from the interaction point present unique challenges in track finding and Particle Identification (PID). For instance, highly displaced protons and pions may bypass the inner pixel detector (PXD) and silicon vertex detector (SVD), leaving hits only in the Central Drift Chamber (CDC). The efficiency of track-finding algorithms as a function of the transverse radius of the decay vertex is heavily dependent on the kinematics of these hadrons.

This study is not intended to compare which hadronization model or form factor approach is better. Instead, we use both the phase-space form factor model and the string/cluster models to study the range of possible track multiplicities and momentum distributions. This helps us understand the phase space and supports the background rejection methods and signal extraction efficiencies used in the rest of the analysis.

Chapter 6

Reconstruction

This chapter contains the variuos steps included in the signal reconstruction.

Baseline Selection

Before vertex reconstruction, event-level criteria ensure data quality and reject trivial backgrounds:

- **Quality & Trigger:** Events must pass standard Belle II quality flags and satisfy at least one hardware (data) or software emulation (MC) hadronic trigger.
- **Track Multiplicity:** A minimum of two reconstructed tracks is required to ensure sufficient activity for vertexing.
- **Luminosity Region:** The interaction point (IP) must be within $r < 2$ cm and $|z| < 5$ cm from the nominal IP.

Veto for Gamma Conversions and K_S^0 Backgrounds

Basic vetoes for conventional backgrounds.

- **Photon Conversions ($\gamma \to e^+e^-$):** We calculate the invariant mass under the electron hypothesis. Combinations with $m_{e^+e^-} < 50$ MeV are rejected.
- K_S^0 **Mesons:** We calculate the invariant mass under the pion hypothesis and veto candidates within $450 < m_{\pi^+\pi^-} < 550$ MeV."

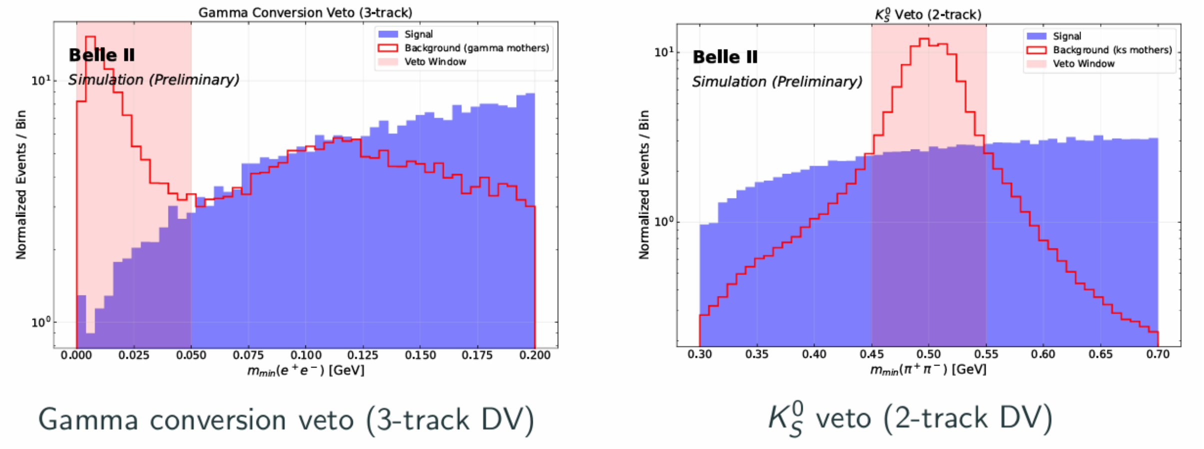

Figure 6.1: Veto distributions for $\gamma \to e^+e^-$ (left) and $K_S^0 \to \pi^+\pi^-$ (right). Shaded regions define the veto windows applied in analysis.

6.1 Displaced Vertex Reconstruction Algorithms

6.1.1 TreeFitter Algorithm

TreeFitter performs a global χ^2 minimization of the decay tree [10]. It forms N-track combinations ($N = 3, 4, 5, 6$) and requires fit convergence, $r_{\text{DV}} > 1.0$ cm, and daughter track $|d_0| > 0.5$ cm relative to the fitted vertex. However, this method is susceptible to double counting, where one track is assigned to multiple overlapping vertex candidates.

6.1.2 Top-Down Track Exclusion Logic

To resolve double counting, an iterative exclusion algorithm is implemented:

1. **Iteration:** The algorithm attempts to fit $N = 6$ vertices first.
2. **Selection & Tagging:** Accepted vertices are selected via a `GlobalVertexSelector`. All constituent tracks are tagged as "used."
3. **Pool Update:** "Used" tracks are removed from the available pool before the algorithm repeats for $N = 5, 4, 3, 2$.

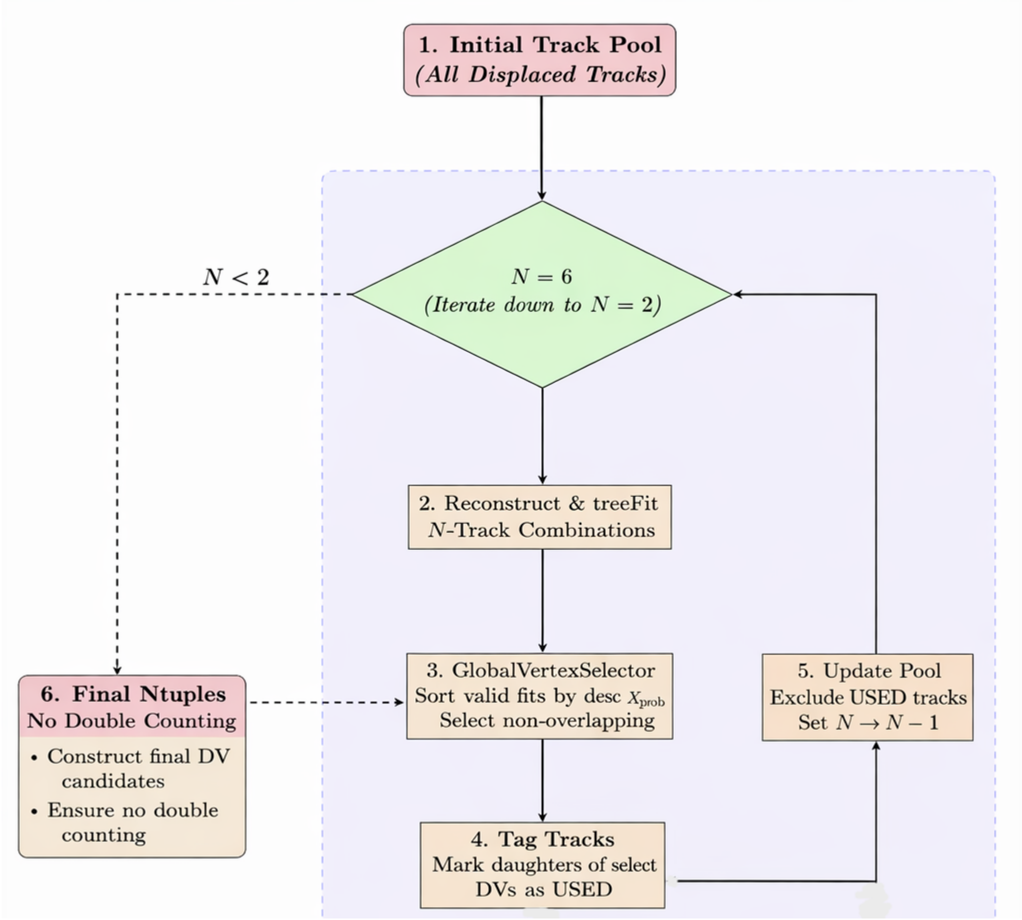

Figure 6.2: Flowchart of the Top-Down Track Exclusion algorithm.

6.2 Invariant Mass Reconstruction and Particle Identification

The invariant mass of the displaced vertex (m_{DV}) serves as very role in the analysis because of potential discriminant from soft background. In this section we analyse relying on the particle ID variables for the tracks to identify get the vertex invariant mass and then check how this affects the mass distribution in signal events and background events.

As the precise identity of the daughter tracks is not known a priori, we rely on the Belle II Particle Identification (PID) variables. To reconstruct the vertex mass, a mass hypothesis is assigned to each track based on its highest PID probability among the standard charged hypotheses (π, K, p, e, μ). we also apply, a strict PID threshold: if the highest ID score for any given track in a vertex falls below 0.6 or 0.9, that track, and subsequently the vertex it belongs to, is removed from the invariant mass calculation. two ID threshold points are taken to see the efficiency and purity trend.

The efficiency of this PID assignment method and the subsequent vertex reconstruction was evaluated using generic $B\bar{B}$ MC. The findings are detailed in Table 6.1 for PID threshold = 0.6 and in Table 6.2 for PID threshold = 0.9. While the efficiency for perfectly identifying all tracks in a vertex drops as multiplicity increases, allowing for a single misidentified track (≤ 1 mis-ID) recovers significant efficiency. We can also see that increasing the PID threshold drops the multiplicity in each region in return giving more efficiency in identifying vertex but if our signal is rare which it is, loosing the multiplicity might not be the good idea.

Table 6.1: Particle Identification and Vertex Reconstruction Efficiencies evaluated on generic $B\bar{B}$ background and signal samples. A PID threshold of 0.6 was required for mass hypothesis assignment.

Sample	**Category**	**Transverse Distance (r_{DV})**	**True / Total Count**	**Efficiency**
Background ($B\bar{B}$)	Individual Tracks	< 5 cm	12,161,134 / 14,726,336	0.8258
		$5 - 20$ cm	161,306 / 192,297	0.8388
		> 20 cm	224,028 / 275,286	0.8138
	Vertex (All tracks correct)	< 5 cm	969,552 / 2,249,139	0.4311
		$5 - 20$ cm	17,999 / 34,766	0.5177
		> 20 cm	22,371 / 48,259	0.4636
	Vertex (≤ 1 mis-ID)	< 5 cm	1,830,291 / 2,249,139	0.8138
		$5 - 20$ cm	30,318 / 34,766	0.8721
		> 20 cm	40,491 / 48,259	0.8390
Signal	Individual Tracks	< 5 cm	71,296 / 80,086	0.8902
		$5 - 20$ cm	24,358 / 29,060	0.8382
		> 20 cm	30,818 / 37,682	0.8178
	Vertex (All tracks correct)	< 5 cm	16,244 / 22,708	0.7153
		$5 - 20$ cm	4,856 / 8,084	0.6007
		> 20 cm	6,391 / 11,367	0.5622
	Vertex (≤ 1 mis-ID)	< 5 cm	21,748 / 22,708	0.9577
		$5 - 20$ cm	7,516 / 8,084	0.9297
		> 20 cm	10,495 / 11,367	0.9233

Table 6.2: Particle Identification and Vertex Reconstruction Efficiencies evaluated on signal and generic $B\bar{B}$ background samples. A PID threshold of 0.9 was required for mass hypothesis assignment.

Sample	**Category**	**Transverse Distance (r_{DV})**	**True / Total Count**	**Efficiency**
Background ($B\bar{B}$)	Individual Tracks	< 5 cm	7,455,875 / 8,280,626	0.9004
		$5-20$ cm	104,341 / 113,361	0.9204
		> 20 cm	138,051 / 154,935	0.8910
	Vertex (All tracks correct)	< 5 cm	468,690 / 719,026	0.6518
		$5-20$ cm	9,568 / 12,621	0.7581
		> 20 cm	11,367 / 16,393	0.6934
	Vertex (≤ 1 mis-ID)	< 5 cm	676,250 / 719,026	0.9405
		$5-20$ cm	12,186 / 12,621	0.9655
		> 20 cm	15,487 / 16,393	0.9447
Signal	Individual Tracks	< 5 cm	53,328 / 56,857	0.9379
		$5-20$ cm	17,184 / 19,096	0.8999
		> 20 cm	21,764 / 25,074	0.8680
	Vertex (All tracks correct)	< 5 cm	12,089 / 14,410	0.8389
		$5-20$ cm	3,263 / 4,335	0.7527
		> 20 cm	4,247 / 6,385	0.6652
	Vertex (≤ 1 mis-ID)	< 5 cm	14,264 / 14,410	0.9899
		$5-20$ cm	4,211 / 4,335	0.9714
		> 20 cm	6,141 / 6,385	0.9618

We will now check the distribution of the invariant mass if this misidentification affects it or not, this is checked only inside the CDC region as more than $r \approx 16\ cm$ would most likely be the cut for our analysis for background suppression of material interaction and other short-lived particle vertices.

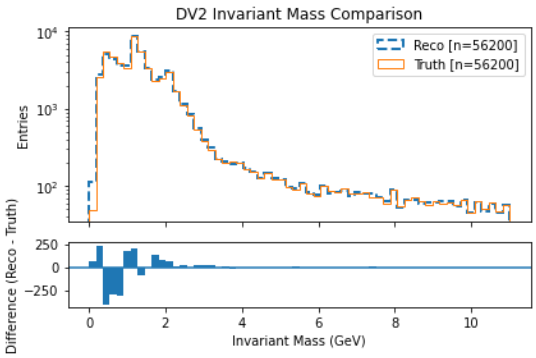

(a) DV2 Signal

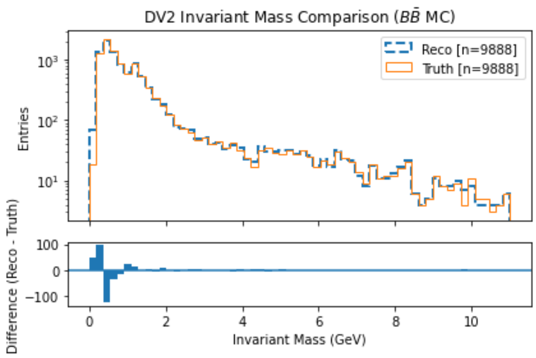

(b) DV2 Background ($B\bar{B}$)

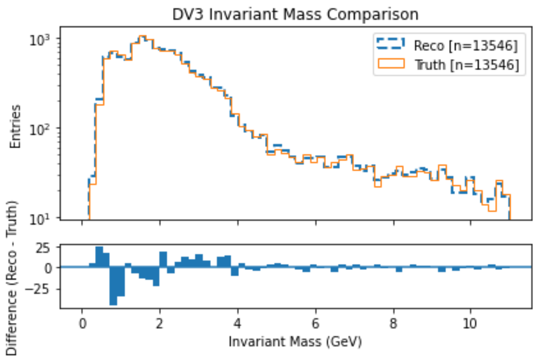

(c) DV3 Signal

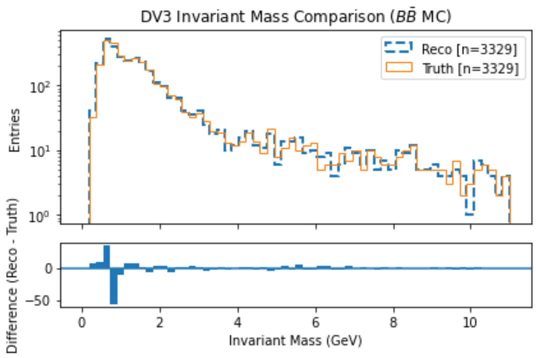

(d) DV3 Background ($B\bar{B}$)

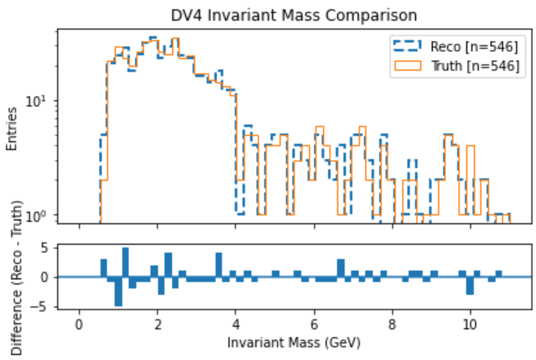

(e) DV4 Signal

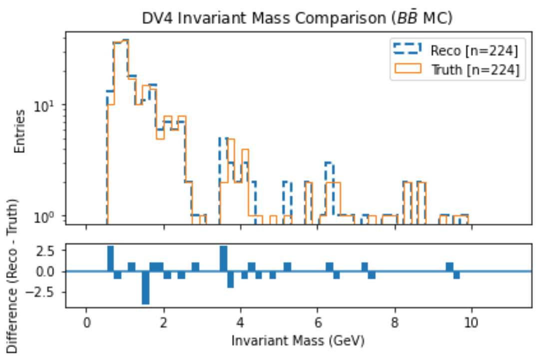

(f) DV4 Background ($B\bar{B}$)

Figure 6.3: Comparison of invariant mass calculated using ID variables of the tracks vs invariant mass calculated using Truth PDG ID of the tracks for the reconstructed vertices. Left column: Signal events, Right column: Background ($B\bar{B}$). Shown for DV2-DV4. (Continued on next figure.)

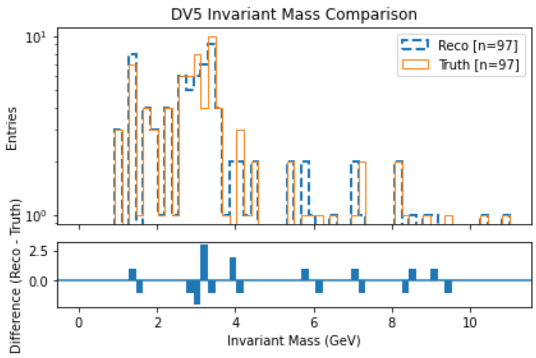

(a) DV5 Signal

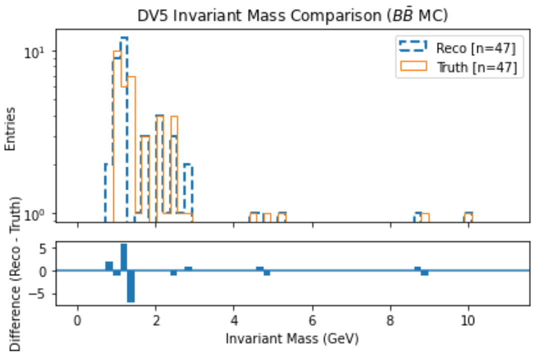

(b) DV5 Background ($B\bar{B}$)

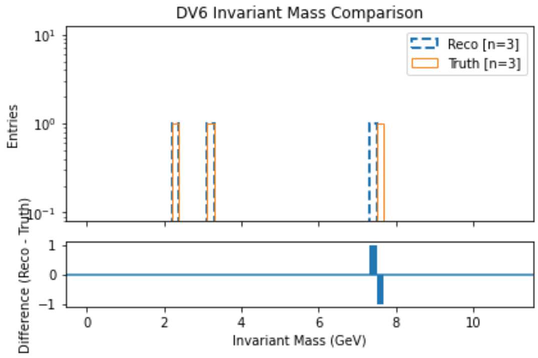

(c) DV6 Signal

Figure 6.4: (Continued.) Comparison of invariant mass calculated using ID variables of the tracks vs invariant mass calculated using Truth PDG ID of the tracks for the reconstructed vertices. Left column: Signal events, Right column: Background ($B\bar{B}$). Shown for DV5-DV6, which has very low statistics in CDC region.

Conclusions

Invariant mass calculated Using best ID variable for tracks, its' efficiency and effect on distribution shown in fig 6.3 and 6.4, This method reconstruction performs reasonably well for lower multiplicity track vertices, however we see some deviations in high mass range in 5 and 6 track vertices, this can be countered with neural network based identification variables. Figure 6.5 contains the comparison with background and signal events.

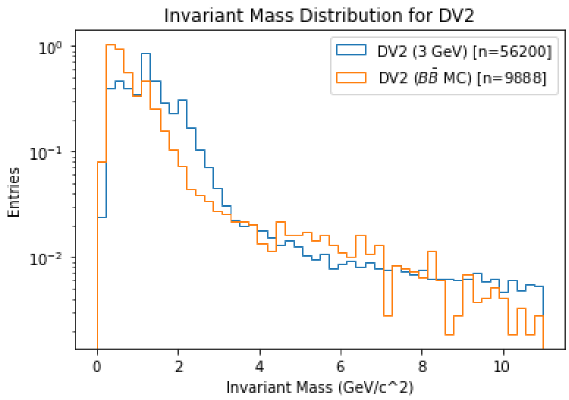

(a) DV2 Invariant Mass Distribution

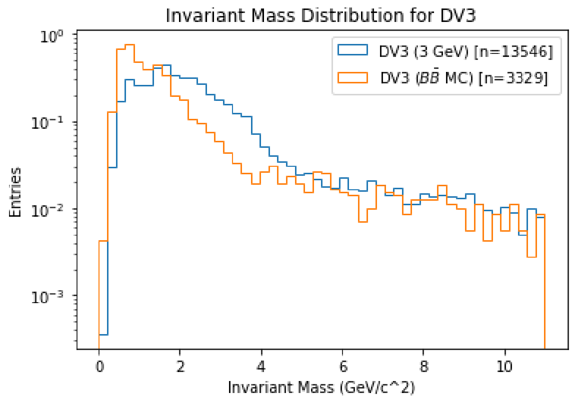

(b) DV3 Invariant Mass Distribution

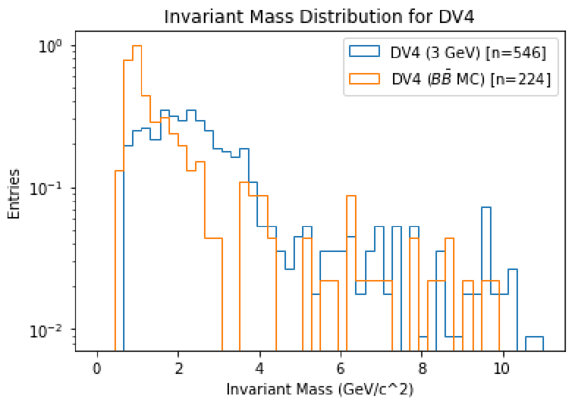

(c) DV4 Invariant Mass Distribution

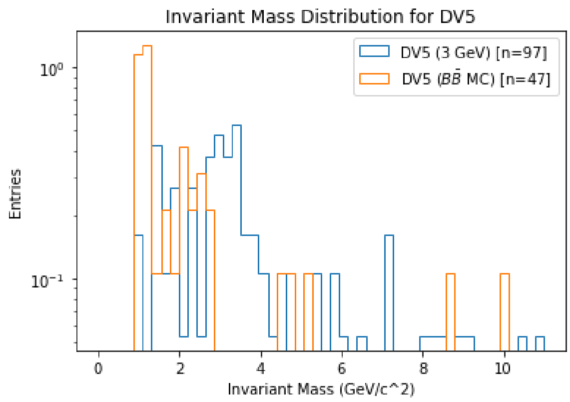

(d) DV5 Invariant Mass Distribution

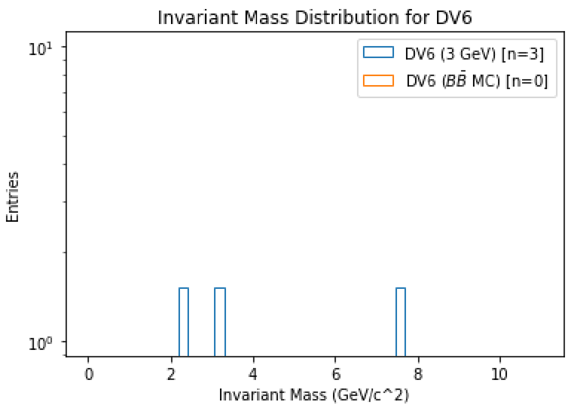

(e) DV6 Invariant Mass Distribution

Figure 6.5: Comparison of invariant mass distributions for signal (3 GeV) and Background ($B\bar{B}$ MC) for reconstructed displaced vertices DV2–DV6.

6.3 Reconstruction of K_S^0 and Λ as Effective Tracks

In our decay cascade, the final state frequently contains long-lived neutral hadrons, namely K_S^0 and Λ, which decay into charged tracks at displaced locations. Since these daughter tracks do not originate directly from the primary displaced vertex (DV) of the neutralino, reconstructing the full decay topology requires treating these particles as single “effective tracks”.

To construct such objects, we first identify high-purity K_S^0 and Λ candidates at the reconstruction level. Signal candidates are defined as those with a true neutralino ancestor, while background candidates arise from generic B decays in Monte Carlo simulations. The study is performed for a benchmark neutralino with $m = 4$ GeV and $c\tau = 7$ m using the full signal statistics (2M events).

6.3.1 Radial Categorization and Observables

The selection is performed in multiple r_{DV} regions due to strong dependence of background composition and detector response on displacement:

$$0 < r_{\mathrm{DV}} < 5 \text{ cm}, \quad 5 < r_{\mathrm{DV}} < 16 \text{ cm}, \quad 16 < r_{\mathrm{DV}} < 24 \text{ cm}, \quad 24 < r_{\mathrm{DV}} < 50 \text{ cm}, \\ r_{\mathrm{DV}} > 50 \text{ cm}$$

The main discriminating variables include:

- dr_{min}: minimum transverse impact parameter of daughter tracks
- $v0\_poca\_ip$: distance of closest approach of V0 trajectory to IP
- $d\phi$: transverse opening angle between momentum and displacement
- $\cos\theta$: 3D pointing angle between momentum and vertex displacement
- fl_{2D}: transverse flight length

6.3.2 Optimized Selection Criteria

The selection cuts are optimized using the Punzi figure of merit [11],

$$F_{\mathrm{Punzi}} = \frac{\epsilon_S}{\frac{5}{2} + \sqrt{B}},$$

with performance validated through ROC curves in each r_{DV} region.

The background and signal statistics vary with radial displacement. Therefore, the optimization is performed separately in multiple r_{DV} bins. In Fig 6.6, all the cuts that have been used is plotted on background rejection vs signal efficiency plane and using punzi figure of merit, the optimal cut has been mentioned beside the plot.

Using these cuts, resulting signal efficiencies (ϵ_S) and background rejection rates are summarized in Table 6.3.

Table 6.3: Summary of optimized selection performance for K_S^0 and Λ candidates across different r_{DV} regions, see Figure 6.6.

r_{DV} region	K_S^0				Λ			
	ϵ_S (%)	Rej. (%)	B	FOM	ϵ_S (%)	Rej. (%)	B	FOM
< 5 cm	64.15	99.07	1344	0.0164	59.51	94.84	556	0.0228
$5 - 16$ cm	85.11	98.34	679	0.0298	74.72	93.35	299	0.0377
$16 - 24$ cm	90.78	98.19	50	0.0948	81.54	90.57	41	0.0916
$24 - 50$ cm	94.39	96.95	28	0.1212	84.77	94.12	11	0.1457
> 50 cm	92.72	95.15	5	0.1958	95.36	100.00	0	0.3814

The results exhibit a clear trend: in the innermost region, constraints on the dominant prompt background looses efficiency. In contrast, the intermediate regions achieve optimal signal–background separation, with signal efficiency exceeding 85% for K_S^0 candidates. At larger displacements, the background is naturally suppressed due to geometric and kinematic constraints, allowing for high signal efficiency with comparatively relaxed selection requirements.

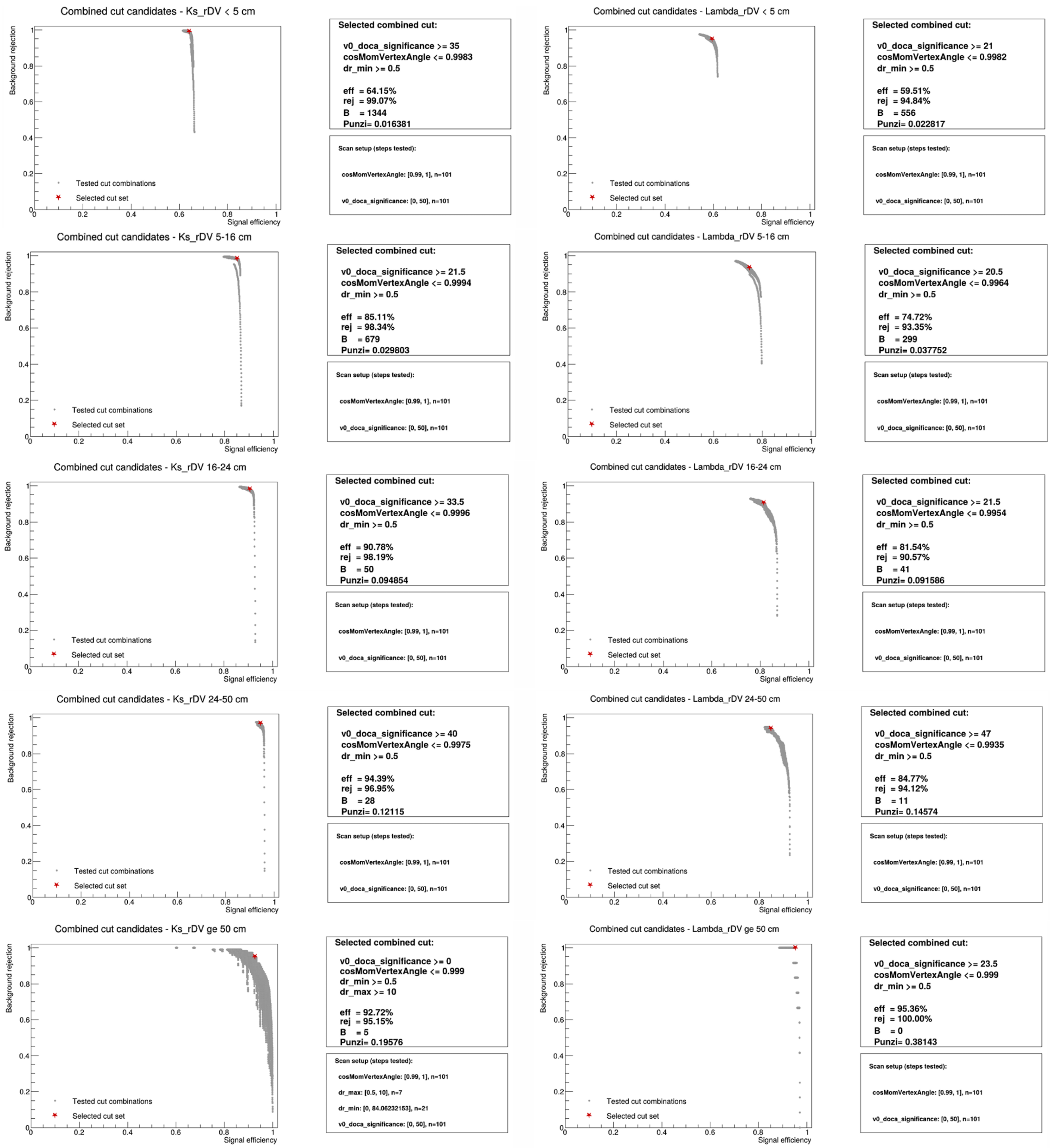

Figure 6.6: Representative optimization results and ROC performance across different r_{DV} regions.

Discussion and Integration into track pool

By applying these rigorously tuned, multi-variable regional cuts, we effectively filter out combinatorial two-track backgrounds and secure a reasonably pure pool of K_S^0 and Λ particles that come from the neutralino decay. These candidates are subsequently merged into the track pool as single effective tracks, allowing the main inclusive vertexer (Section 6.1) to reliably reconstruct the true multi-prong topology of the neutralino decay.

6.4 Association with Prompt Λ and Protons

The signal process follows the topology $B \to \Lambda/p + X$, where X is a long-lived neutralino. To isolate the signal, the reconstructed displaced vertex (DV) must be associated with a prompt Λ baryon or proton from the primary interaction point (IP).

Prompt Particle Identification

- **Prompt Λ:** Reconstructed from $\Lambda \to p\pi^-$ with a vertex $r_{\mathrm{V0}} < 2$ cm. The invariant mass must satisfy $|m_{p\pi} - m_\Lambda| < 10$ MeV, supplemented by daughter track PID.
- **Prompt Protons:** Identified via Belle II PID (likelihood > 0.9) with a transverse impact parameter $|d_0| < 0.1$ cm.

Constraints The reconstructed B-meson candidate is required to satisfy consistency conditions based on the beam energy in the center-of-mass (CM) frame. Variables for selection:

- **Energy Difference:**
$$\Delta E = E_B^* - E_{\mathrm{beam}}^* \tag{6.1}$$
where E_B^* is the reconstructed energy of the B candidate and E_{beam}^* is the beam energy in the CM frame. Signal candidates are expected to peak near $\Delta E \approx 0$.

- **Beam-Constrained Mass:**
$$M_{\mathrm{bc}} = \sqrt{(E_{\mathrm{beam}}^*)^2 - |\vec{p}_B^{\,*}|^2} \tag{6.2}$$
where $\vec{p}_B^{\,*}$ is the reconstructed momentum of the B candidate in the CM frame. Signal events peak at the nominal B-meson mass.

Selection windows are applied:

$$|\Delta E| < \mathcal{O}(0.05\text{–}0.1)\ \mathrm{GeV}, \tag{6.3}$$
$$5.27\ \mathrm{GeV} < M_{\mathrm{bc}} < 5.29\ \mathrm{GeV}. \tag{6.4}$$

-

This association constitutes the final selection stage. Only candidates consistent with the $B \to \Lambda/p + \mathrm{DV}$ topology and satisfying all kinematic constraints are retained for signal extraction and statistical analysis.

Chapter 7

Background Studies

A fundamental challenge in the inclusive search for displaced vertices (DVs) is the presence of SM processes that can closely mimic the signal signature. The signal topology targeted in this analysis consists of a long-lived particle (such as an R-parity violating neutralino) decaying into a multi-track displaced vertex with a track multiplicity of $N_{\text{tracks}} \geq 4$, accompanied by a prompt baryon originating from the primary B meson decay. Because the search is inclusive, meaning it does not fully reconstruct the entire event kinematics, that way we can have 2 or 3 tracks signal vertices as well, but one would expect very high background in such case. Consequently, several background sources, ranging from neutral hadron decays to particle-material interactions, must be estimated and suppressed accordingly.

Overview of Background Sources

Before applying specialized selection criteria, the background that satisfies the basic displaced vertex requirements can be categorized into three primary physical origins.

The first category comprises V0-like decays, which are the prompt weak decays of long-lived SM neutral hadrons, primarily $K_S^0 \to \pi^+\pi^-$ and $\Lambda \to p\pi^-$. While these processes naturally produce two-track vertices, they are overwhelmingly abundant in generic $B\bar{B}$ events. They can easily form higher-multiplicity background vertices through accidental track crossings, either with other displaced tracks or with prompt tracks originating from the interaction point (IP). Similarly, photon conversions ($\gamma \to e^+e^-$) in the detector material lead to low-mass displaced vertices that must be vetoed.

The second major category involves genuine multi-track displaced vertices originating from the weak decays of heavy-flavor and strange Standard Model particles. Unlike the accidental combinatorial crossings of two-track V0s, these processes inherently yield three or more charged tracks. Prominent sources within generic $B\bar{B}$ events include the decays of charmed hadrons (such as D^0, D^+, D_s^+, and Λ_c^+) and strange baryons (hyperons).

For charmed hadrons, the characteristic decay lengths ($c\tau$) are typically on the order of 100 to 300 μm. While this is significantly shorter than the nominal signal displacement requirement of $r_{\mathrm{DV}} > 1$ cm, the extreme tails of their exponential lifetime distributions can occasionally extend well into the fiducial signal volume. Because they naturally decay into higher-multiplicity hadronic final states (for instance, $D^0 \to K^-\pi^+\pi^+\pi^-$) and possess relatively high invariant masses, they represent a genuine topological background, albeit one heavily suppressed at large radii.

Conversely, hyperons, such as Ξ^-, Σ^-, Ξ^0, and Ω^-, have much longer lifetimes, typically on the order of 0.1 ns ($c\tau \sim 3$ cm). This naturally places their decay vertices squarely within the displaced signal region without relying on lifetime tails. However, the probability of these hyperons mimicking a genuine multi-track signal is mitigated by their decay topologies and branching ratios. Most hyperons do not have significant direct $\geq$ 3-track decay modes. Instead, potential 3-track and 4-track backgrounds arise primarily from cascade decays, such as $\Xi^- \to \Lambda\pi^-$ followed by $\Lambda \to p\pi^-$, or similar cascades from Ω^- and Ξ^0.

Because the intermediate daughter particle (e.g., the Λ baryon) is itself long-lived, the final state tracks do not physically originate from a single spatial point. Rather, they form two distinct, separated vertices. This geometric separation provides a natural handle for suppression; enforcing strict vertex fit quality criteria (χ^2 probability) and ensuring all tracks in the candidate originate from a common point effectively rejects these hyperon cascades. Furthermore, any ultra-rare direct 3-track decays (e.g., potential Σ^- multi-body modes) suffer from exceedingly small branching fractions, minimizing their overall rate in the data. Careful Monte Carlo studies, particularly focusing on two-body B decays, are utilized to map and evaluate any residual contributions from these hyperon cascades.

The other major category involves material interactions. When high-energy hadrons traverse the inner components of the detector, such as the beam pipe and the inner walls of the Central Drift Chamber (CDC), they can undergo hadronic interactions or annihilations. These interactions naturally produce high-multiplicity displaced vertices that are phenomenologically very similar to the decay of a heavy long-lived particle. Preliminary Monte Carlo (MC) truth studies on generic B^+B^- samples indicate that for 3-track DVs, antinucleon interactions are the dominant background contributors. Specifically, before material or mass vetoes are applied, antiprotons ($\bar{p}$) account for approximately 44% of the total tracks, while antineutrons ($\bar{n}$) account for roughly 17%, as shown in the Fig. 7.1 (plot generated by Bogdan Kutsenko). Also note that this plot is made from truth MC for estimation.

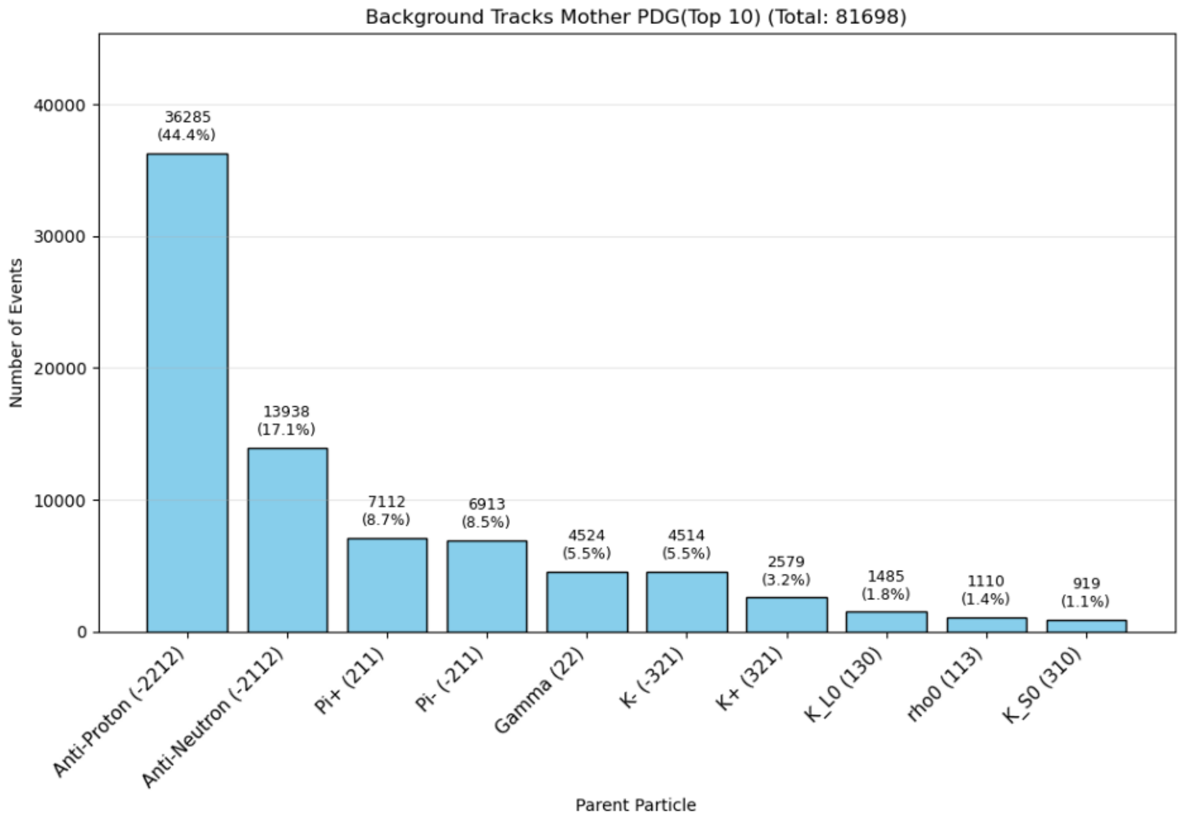

Figure 7.1: For 3 tracks vertices, this plot shows count of a track's mother PID

The final category is combinatorial background, which arises from the accidental crossing of unrelated tracks that happen to satisfy the vertexing algorithm's spatial and kinematic criteria, producing a fake multi-track vertex.

Displaced Track Selection and Quality Requirements

To isolate tracks that genuinely originate from long-lived particles, it is first necessary to suppress the extremely high-density prompt background originating directly from the IP. We achieve this by applying strict geometric and detector-level criteria to all individual tracks before they are considered for vertex fitting.

Prompt tracks are initially filtered using their transverse (d_r) and longitudinal (d_z) impact parameters. By requiring tracks to be significantly displaced from the primary interaction point, the vast majority of prompt background is eliminated. Based on comparisons between signal and generic MC distributions, we require a longitudinal displacement of $|d_z| > 1.0$ cm and a transverse displacement of $|d_r| > 0.5$ cm, as shown in fig 7.2 (plots generated by Bogdan Kutsenko). The transverse cut, in particular, completely removes the core prompt background peak at the IP.

Further discrimination is achieved by exploiting hit information from the Belle II

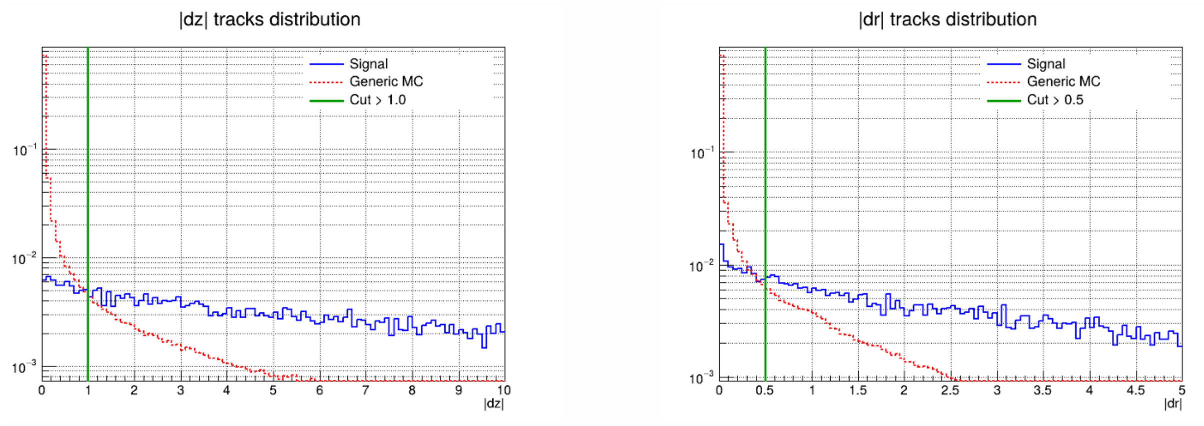

Figure 7.2: Distributions of the longitudinal ($|d_z|$, left) and transverse ($|d_r|$, right) impact parameters for tracks in signal (Neutralino 4 GeV, $c\tau = 7$ m)compared to generic $B\bar{B}$ MC16ri, $0.511ab^{-1}$.

tracking detectors. Since signal vertices are displaced radially outwards ($r_{\mathrm{DV}} > 1$ cm), the daughter tracks originating from these vertices should not physically traverse the innermost layers of the detector. Therefore, we impose a Pixel Detector (PXD) hit veto, requiring that candidate displaced tracks have zero hits in the innermost PXD layers ($nPXDHits < 1$). Additionally, because displaced tracks originate further from the IP, their path length through the Central Drift Chamber is shorter, resulting in a systematically lower number of CDC hits ($nCDCHits$) compared to prompt tracks. These detector-level observables provide a robust secondary filter against tracks that have been misreconstructed or have large impact parameters.

7.1 Material Interactions and Antinucleon Annihilation

As established from MC truth studies, interactions of particles with the detector material pose a formidable challenge because they produce genuine high-multiplicity, high-mass displaced vertices. The regions of highest concern are the beam pipe (radially located at approximately 1.0 to 1.2 cm) and the inner wall of the CDC.

To understand the scope of this background, an analytical estimation of antiproton ($\bar{p}$) annihilation in the CDC gas was performed. The CDC utilizes a gas mixture of 50% Helium and 50% Ethane (C_2H_6) by volume. By applying the ideal gas law ($PV = NkT$) at 0.5 atmospheres for Ethane at 300 K, the molecular density is calculated. Considering that an ethane molecule contains 30 nucleons and ignoring the lighter helium contribution, the nucleon density (N_N/V) is approximately 3.6×10^{25} nucleons/m^3.

For an antinucleon traversing a roughly 1-meter path length through the CDC, the number of nucleons per unit area is 3.6×10^{25} m^{-2}. Assuming an annihilation cross-section of roughly 50 mb for producing an event with 4 or more prongs (tracks), the interaction probability R is given by:

$$R = \sigma \cdot \left(\frac{N_N}{A}\right) \approx \left(0.05 \times 10^{-28}\ \text{m}^2\right) \times \left(3.6 \times 10^{25}\ \text{m}^{-2}\right) = 0.18 \times 10^{-4} \tag{7.1}$$

Previous precision measurements by CLEO [12] and ARGUS [13] indicate that a proton or antiproton is present in about 8% of all B decays, This was done inclusively, i.e., a proton or antiproton was found in 16% of BB events. Half of these are antiprotons, so there is an antiproton in 8% of BB events Given the vast number of $B\bar{B}$ pairs produced at Belle II, this interaction probability results in a statistically significant background of multi-track vertices.

Because these annihilations occur strictly where material is present, mapping the physical (x, y) coordinates of reconstructed background vertices provides a clear 2D image of the detector structures. Vertices falling within these highly populated material bands are subject to a stringent geometric material veto. Figures 7.3 to 7.7 (plots generated by Bogdan Kutsenko) show the material interaction map of these vertices. we see for 2-track vertices the count is too high, even in CDC region, our initial plan is to remove it from the analysis. Work is in-progress for mitigation of higher multiplicity vertices.

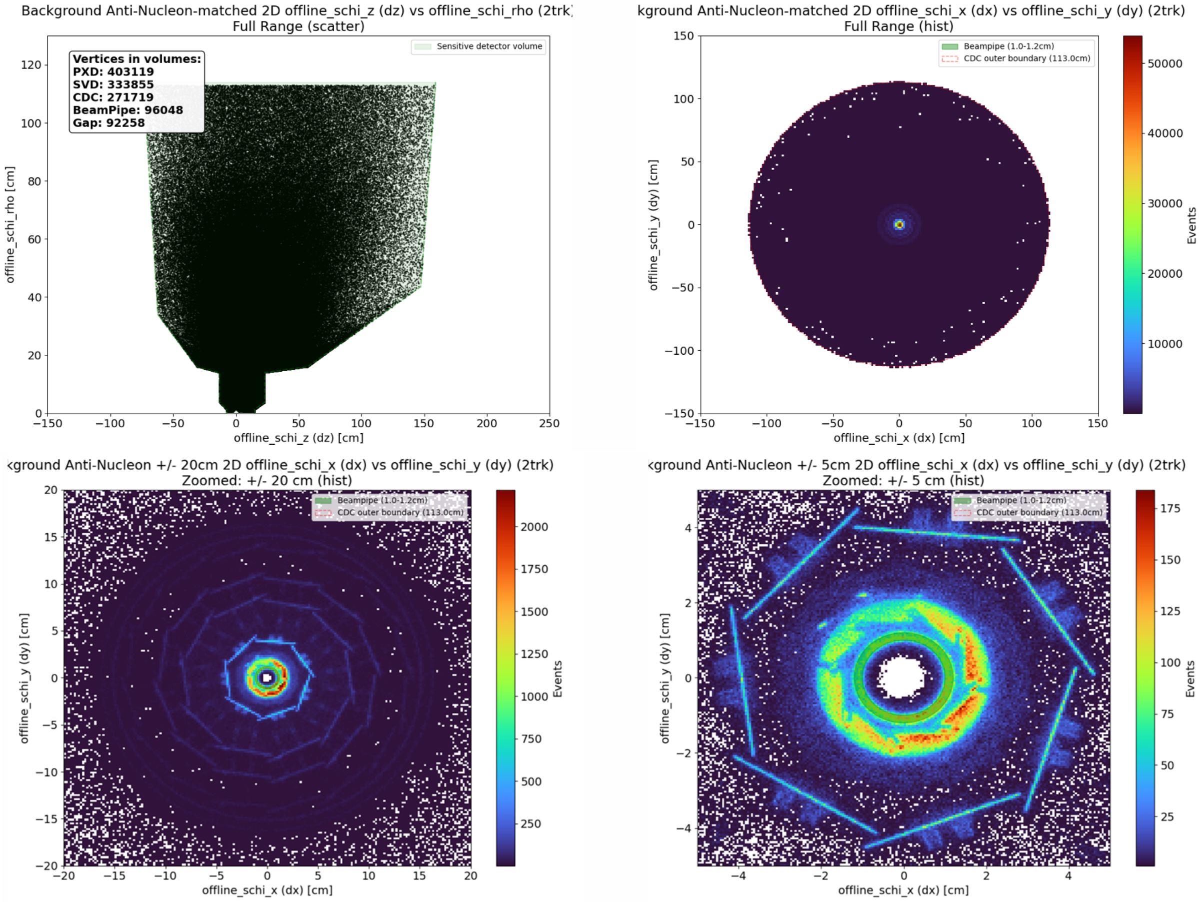

Figure 7.3: 2 track vertices due to anti-nucleon are shown in different planes, Top: ρZ plane, Bottom: XY plane.

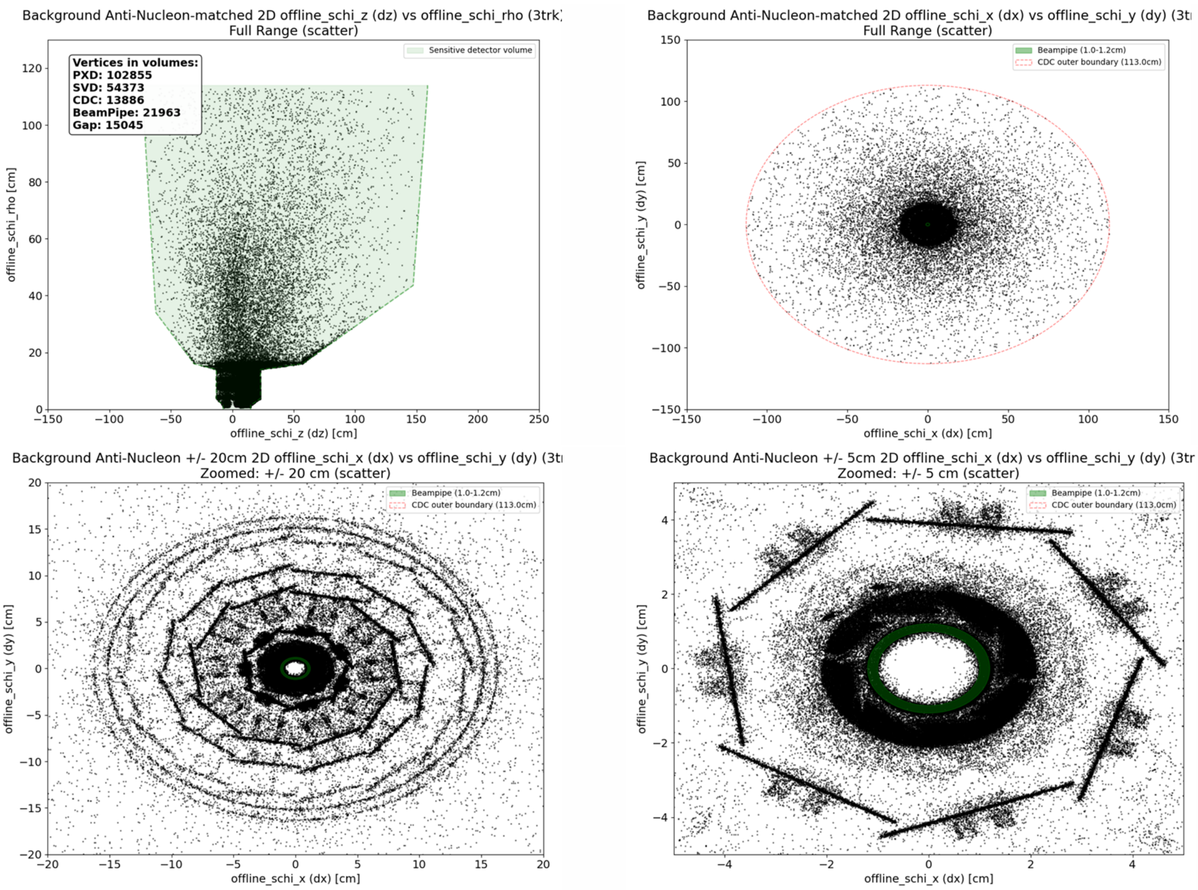

Figure 7.4: 3 track vertices due to anti-nucleon are shown in different planes, Top: ρZ plane, Bottom: XY plane.

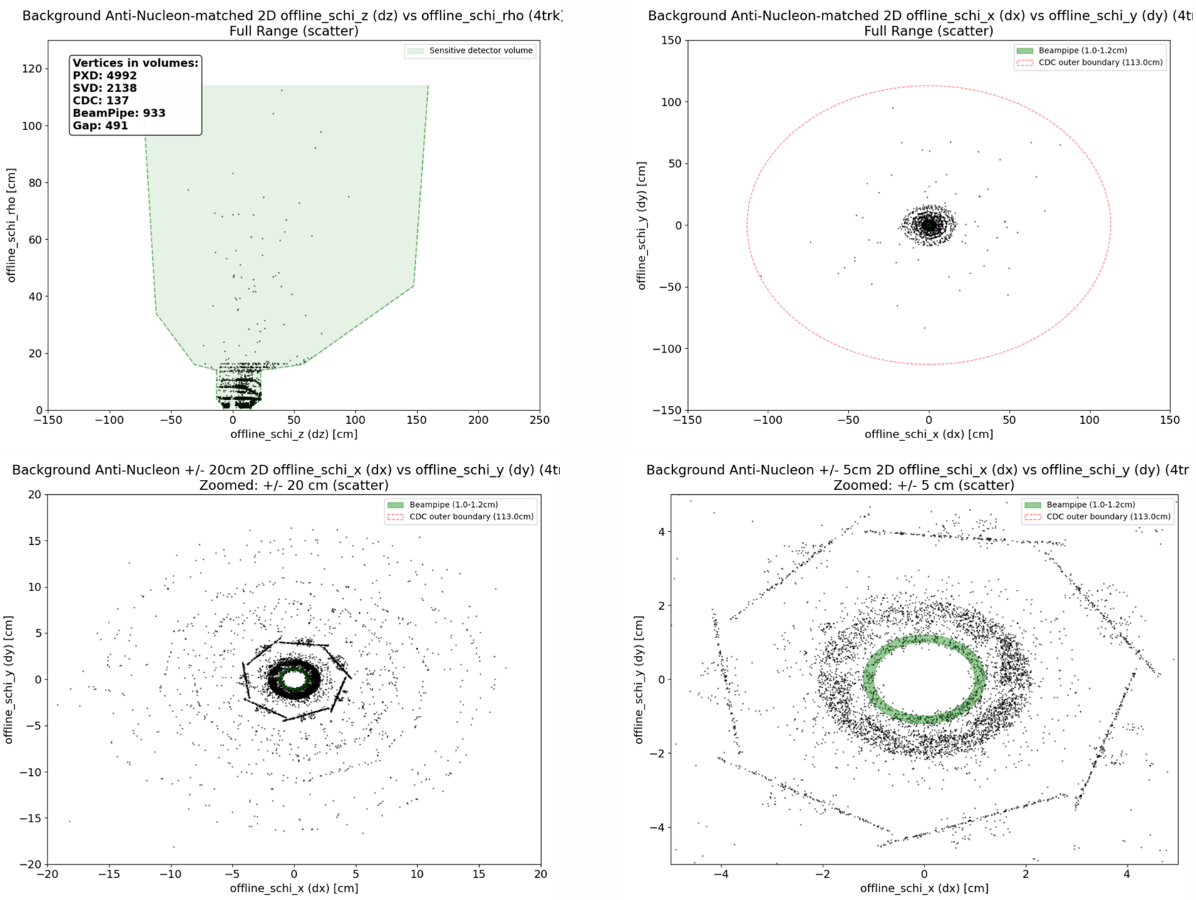

Figure 7.5: 4 track vertices due to anti-nucleon are shown in different planes, Top: ρZ plane, Bottom: XY plane.

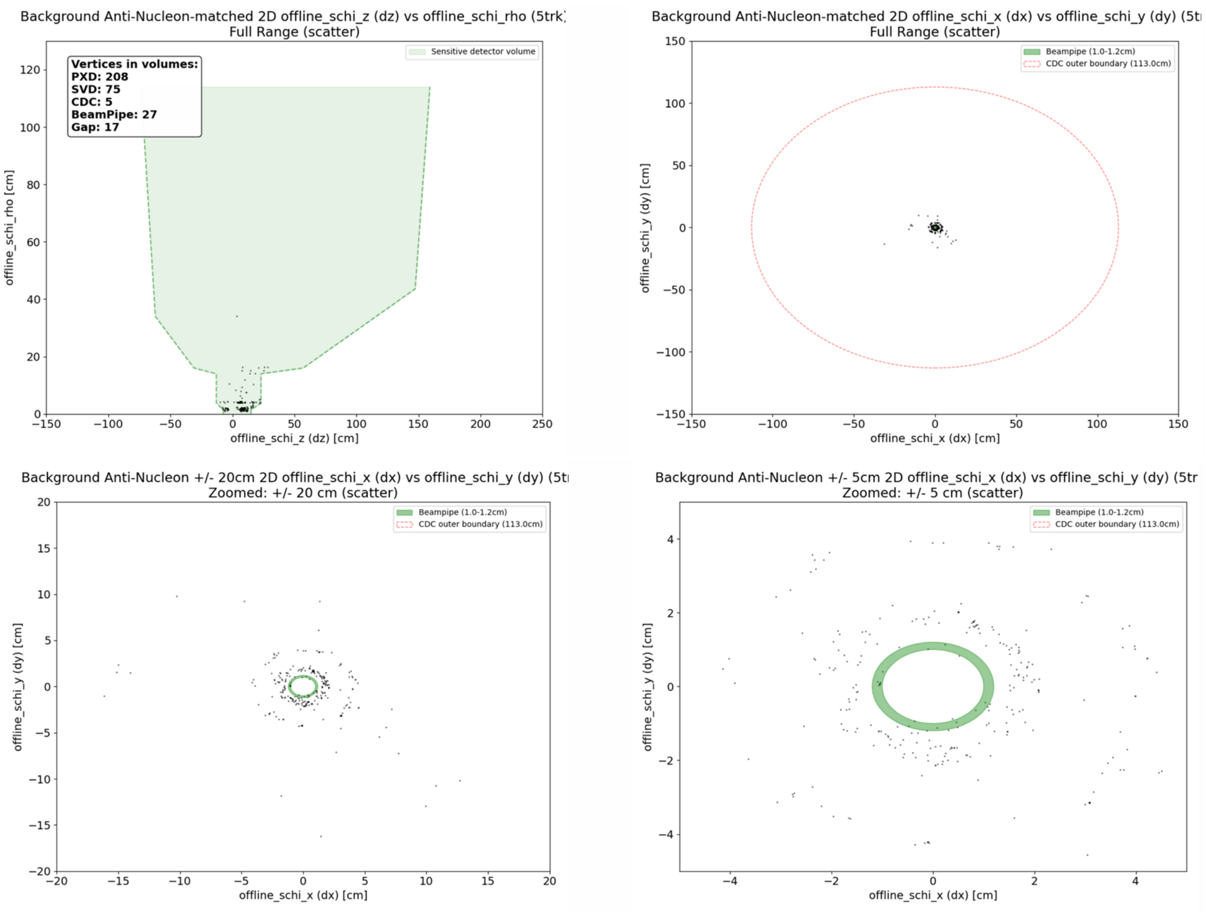

Figure 7.6: 5 track vertices due to anti-nucleon are shown in different planes, Top: ρZ plane, Bottom: XY plane.

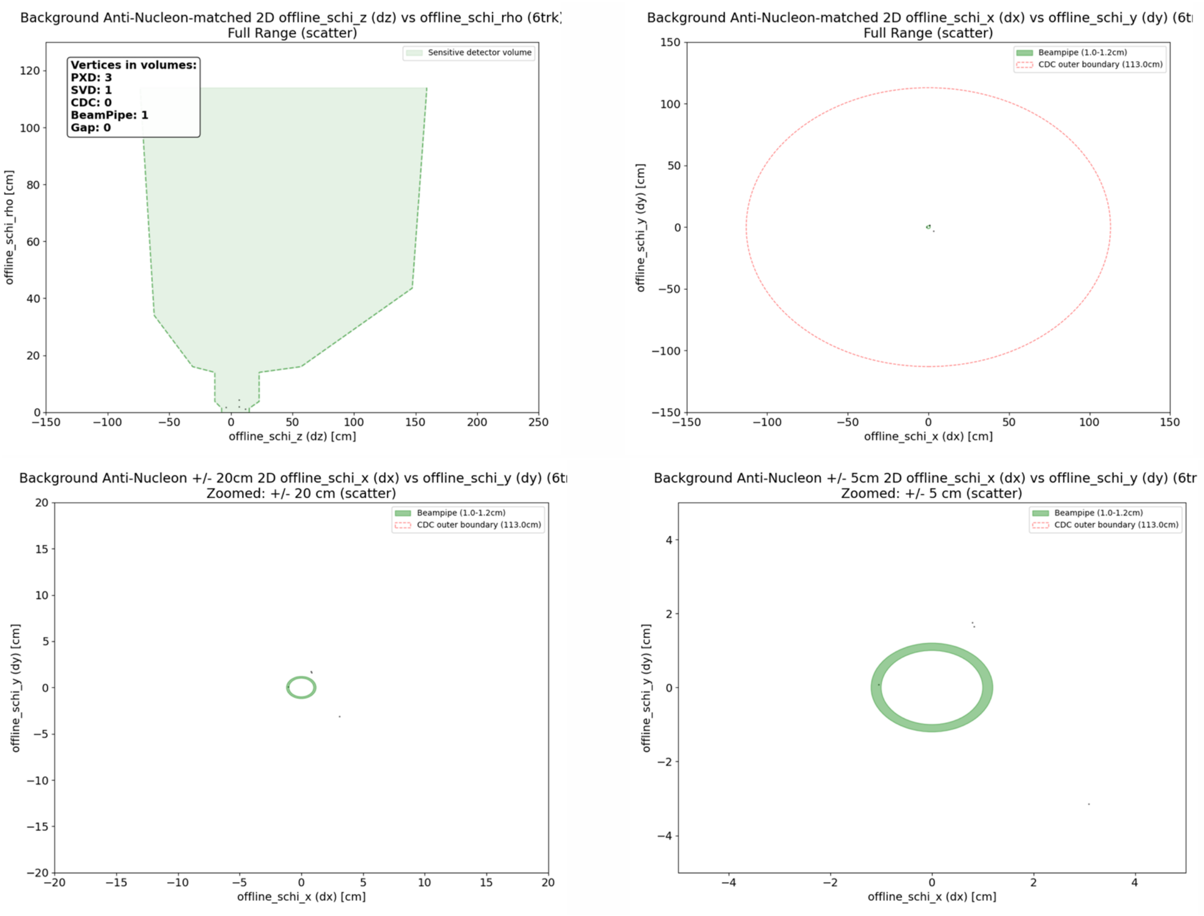

Figure 7.7: 6 track vertices due to anti-nucleon are shown in different planes, Top: ρZ plane, Bottom: XY plane.

7.2 Cut based Analysis on Daughter-Track Variables

In this chapter, we discuss the cut based rejection of the background vertices, note that this analysis is done more realistically, without knowing if vertex is truly from the neutralino or not, but required that it is in the signal event.

Definition of daughter-track difference variables For a vertex with multiple daughter tracks, the difference variables (e.g. Δd_0, Δz_0) are computed pairwise between all track combinations. From these, we define:

- ΔX_{min}: the minimum difference among all track pairs,
- ΔX_{max}: the maximum difference among all track pairs.

The selection is applied independently on these quantities:

$$\Delta X_{\text{min}} > \text{min\_cut}, \quad \Delta X_{\text{max}} > \text{max\_cut}. \tag{7.2}$$

For two-track vertices (DV2), there is only one pair, and hence $\Delta X_{\min} = \Delta X_{\max}$. For higher multiplicities such as DV3, these correspond to different track combinations and provide additional discrimination power.

7.2.1 Two-Track Vertices (DV2)

We begin by studying daughter-track level variables for two-track displaced vertices. The goal is to identify observables that provide discrimination between signal-like vertices (originating from neutralino decays) and background vertices, without using truth-level information. The optimisation is performed using a cut-based approach, maximising the figure of merit

$$\text{FoM} = \frac{\epsilon_S}{\frac{5}{2} + \sqrt{B}}. \tag{7.3}$$

The distributions of the daughter-track difference variables are shown below.

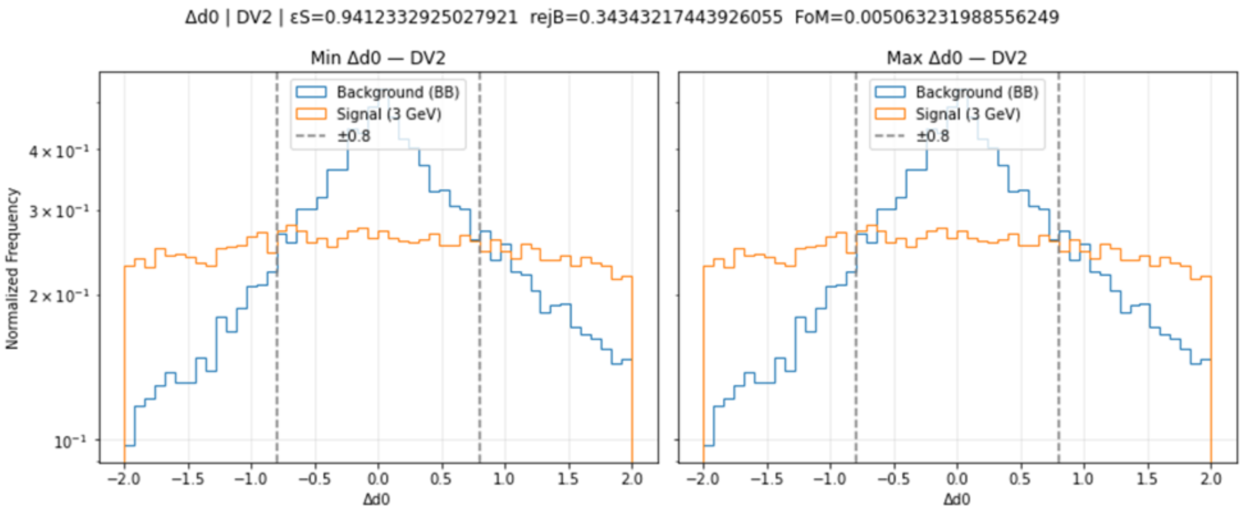

Figure 7.8: Distribution of Δd_0 for signal and background in DV2 vertices.

Dominant discriminating variable: Δd_0 The transverse impact parameter difference between the two daughter tracks, Δd_0, provides the strongest discrimination power. A cut of

$$\Delta d_0 > 0.8 \tag{7.4}$$

gives:

$$\epsilon_S = 0.94, \tag{7.5}$$

$$\text{Background rejection} = 0.34, \tag{7.6}$$

$$\text{FoM} = 5.06 \times 10^{-3}. \tag{7.7}$$

This remains the only variable that significantly improves the signal-to-background separation for DV2 vertices.

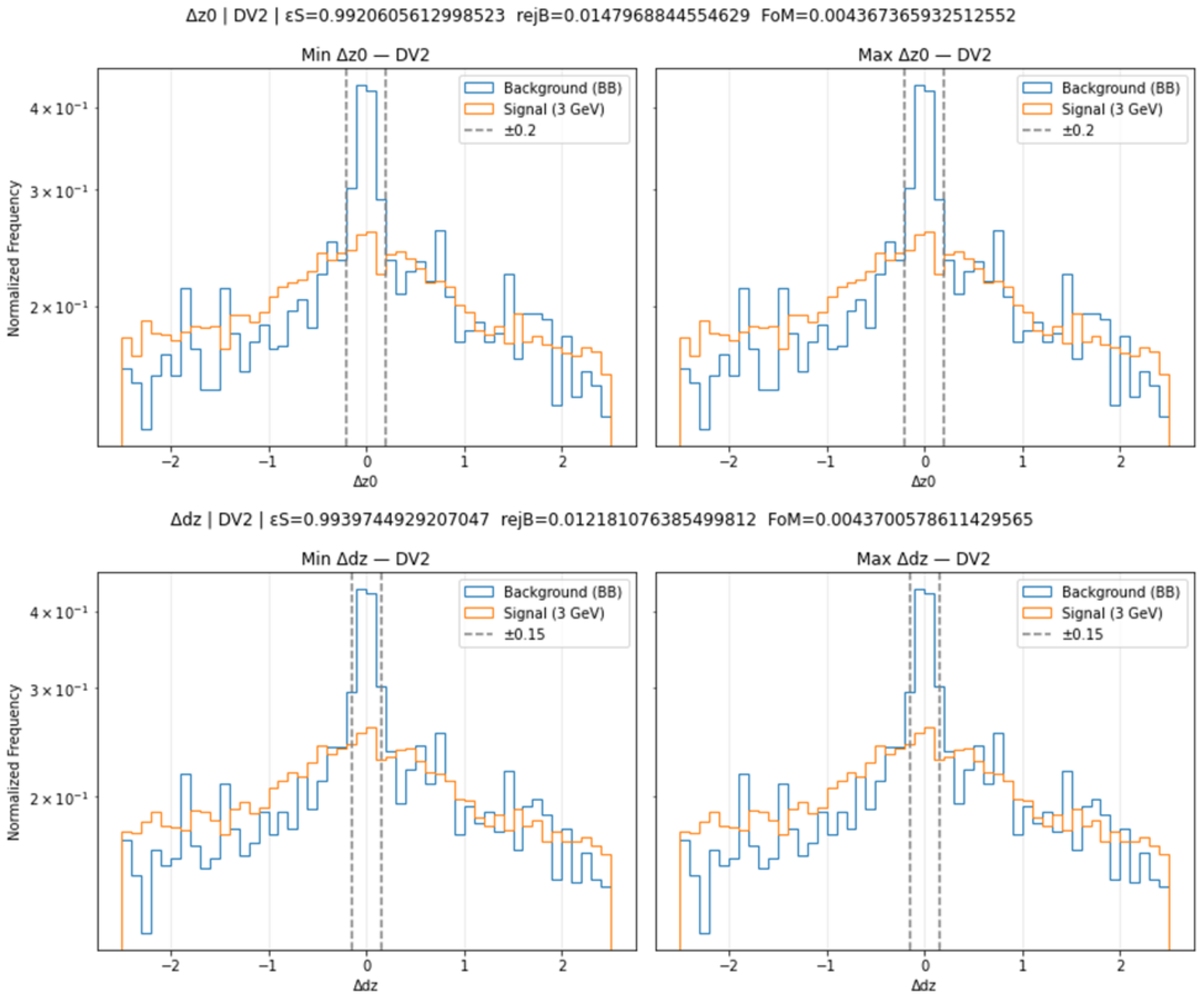

Figure 7.9: Distributions of Δz_0 (left) and Δd_z (right) for DV2 vertices.

Subleading variables: Δz_0 and Δd_z The longitudinal impact parameter difference Δz_0 and separation along the beam direction Δd_z show only marginal discrimination. The optimal cuts are:

$$\Delta z_0 > 0.2, \quad \Delta d_z > 0.15, \tag{7.8}$$

with performance:

$$\epsilon_S \sim 0.99, \tag{7.9}$$

$$\text{Background rejection} \sim 0.01, \tag{7.10}$$

$$\text{FoM} \approx 4.37 \times 10^{-3}. \tag{7.11}$$

These variables do not significantly enhance the overall sensitivity.

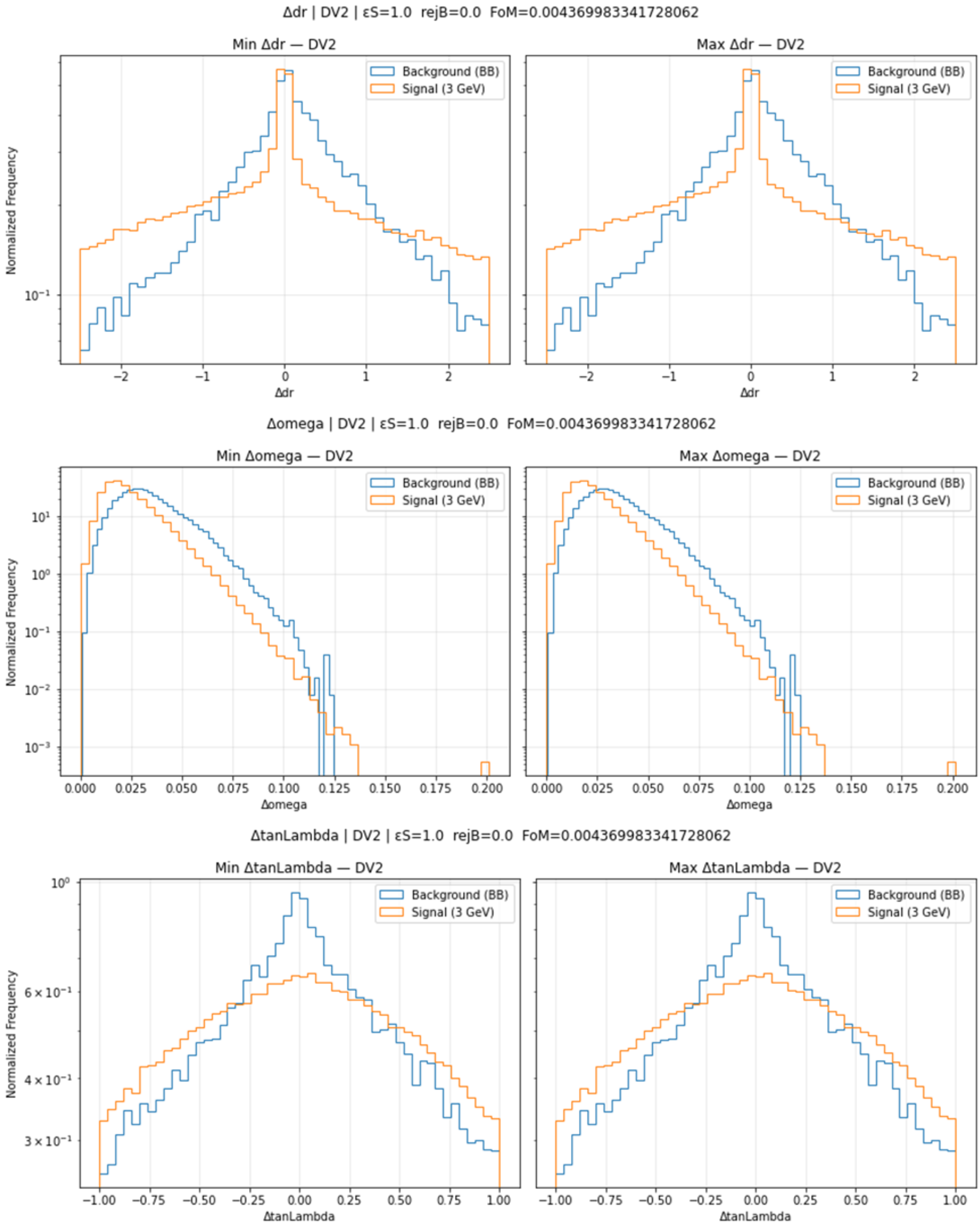

Figure 7.10: Distributions of Δdr, $\Delta\omega$, and $\Delta\tan\lambda$ for DV2 vertices. No significant separation is observed.

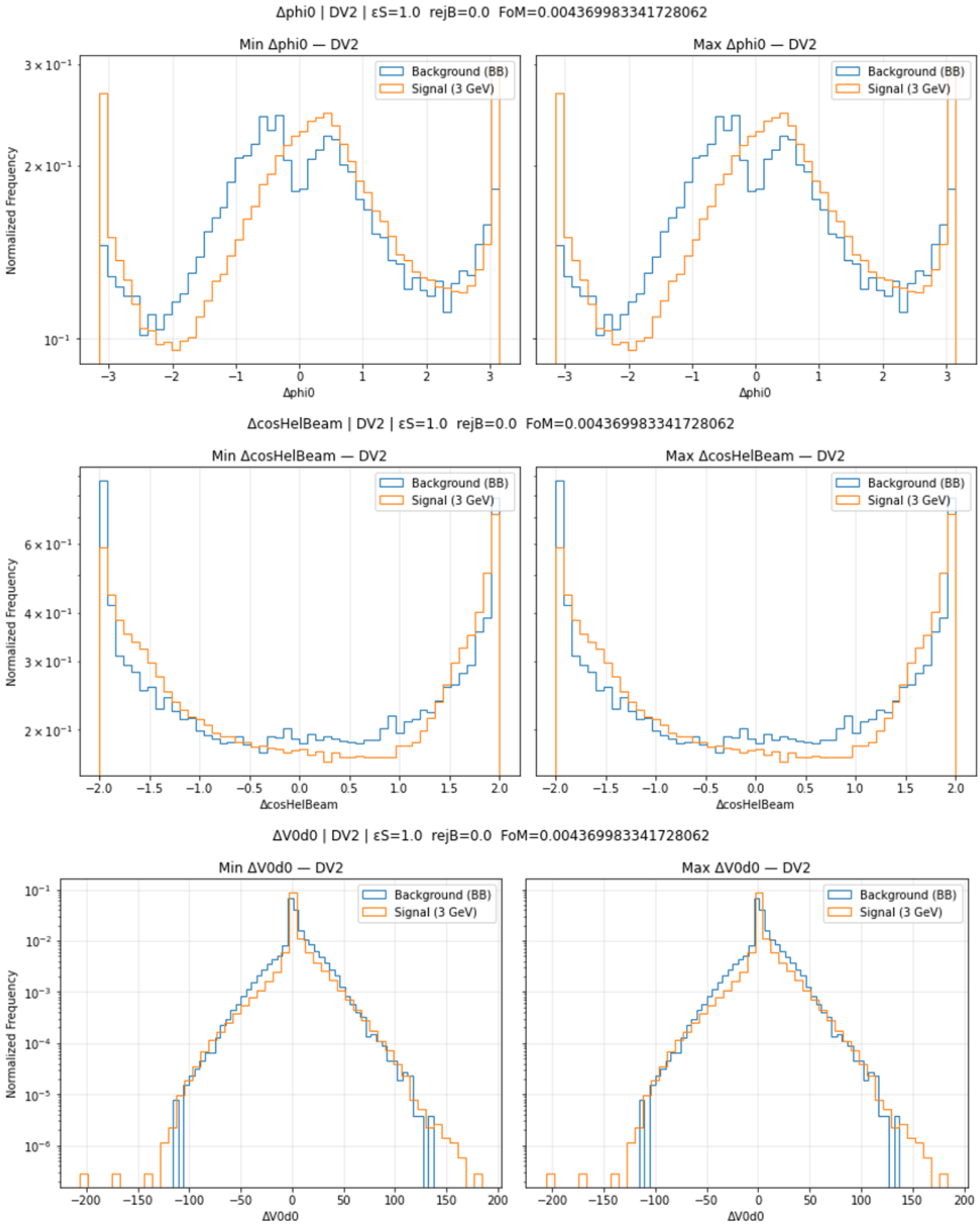

Figure 7.11: Distributions of $\Delta\phi_0$, $\Delta\cos\theta$, and Δd_0^{V0} for DV2 vertices. No significant separation is observed.

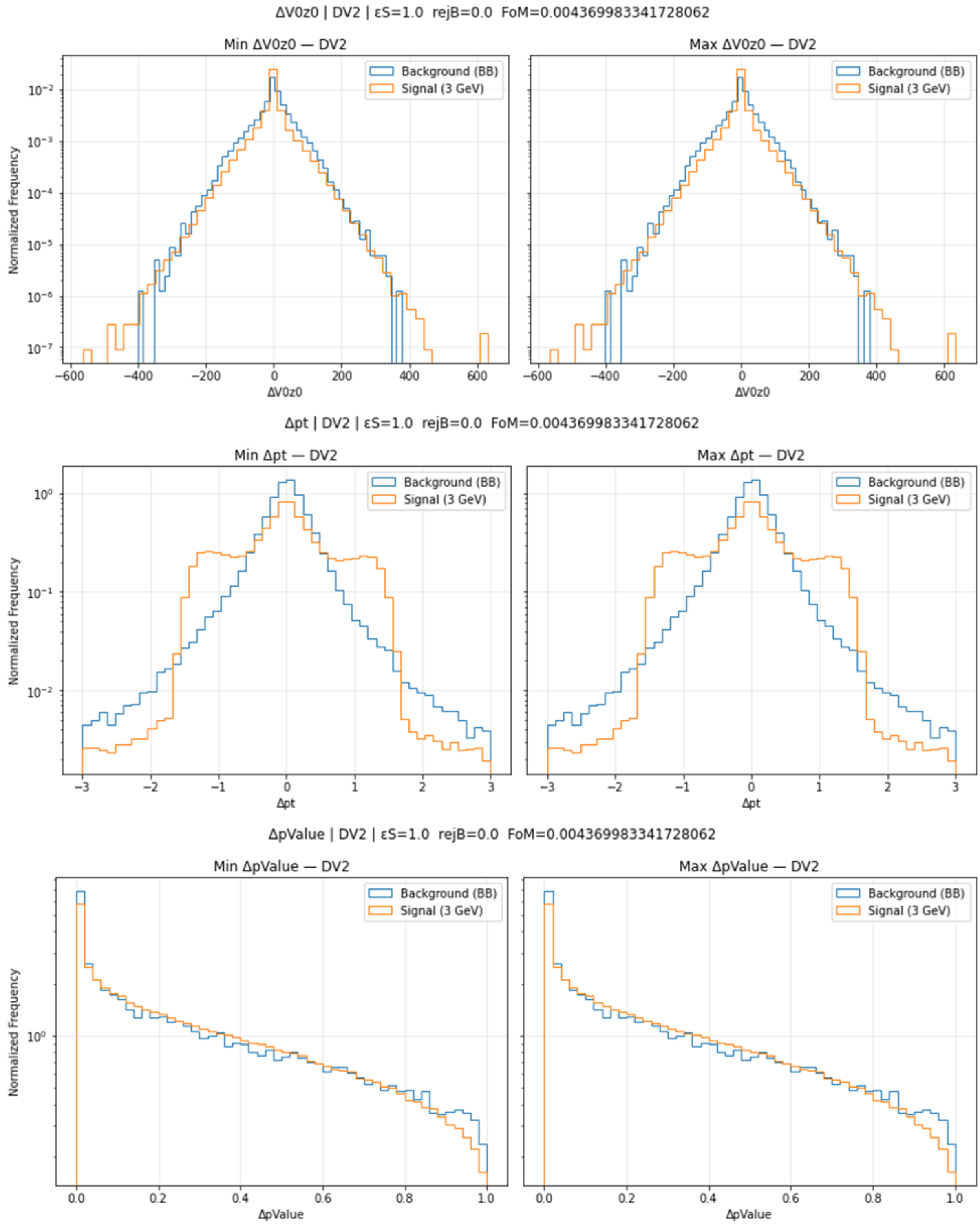

Figure 7.12: Distributions of Δz_0^{V0}, Δp_T, and Δp-value for DV2 vertices. No significant separation is observed.

Non-discriminating variables All remaining variables shown in 7.10, 7.11 and 7.12:

$$\epsilon_S = 1, \quad \text{Background rejection} = 0, \quad \text{FoM} \approx 4.37 \times 10^{-3}. \tag{7.12}$$

Combined performance Combining all variables sequentially, the overall selection yields:

$$\epsilon_S^{\text{combined}} = 0.934, \tag{7.13}$$

$$\text{Background rejection}^{\text{combined}} = 0.35, \tag{7.14}$$

with:

$$\text{FoM} = 5.04 \times 10^{-3}, \quad S/B \approx 12.4. \tag{7.15}$$

The combined performance is still dominated by the Δd_0 cut, with negligible contributions from other variables.

The results for the most relevant variables are summarised in Table 7.1.

Variable	Cut	ϵ_S	Background rejection	FoM
Δd_0	> 0.8	0.94	0.34	5.06×10^{-3}
Δz_0	> 0.2	0.99	0.01	4.37×10^{-3}
Δd_z	> 0.15	0.99	0.01	4.37×10^{-3}
Combined	–	0.93	0.35	5.04×10^{-3}

Table 7.1: Summary of cut performance for daughter-track variables in two-track vertices using the modified FoM definition.

Overall, for two-track vertices, daughter-track level variables provide very limited discrimination. The separation is driven almost entirely by Δd_0, while all other variables contribute negligibly.

7.2.2 Three-Track Vertices (DV3)

We now extend the analysis to three-track displaced vertices. Compared to DV2, the additional track allows multiple pairwise combinations, enabling the definition of minimum and maximum differences between daughter tracks. These provide stronger geometric constraints and improved discrimination between signal and background.

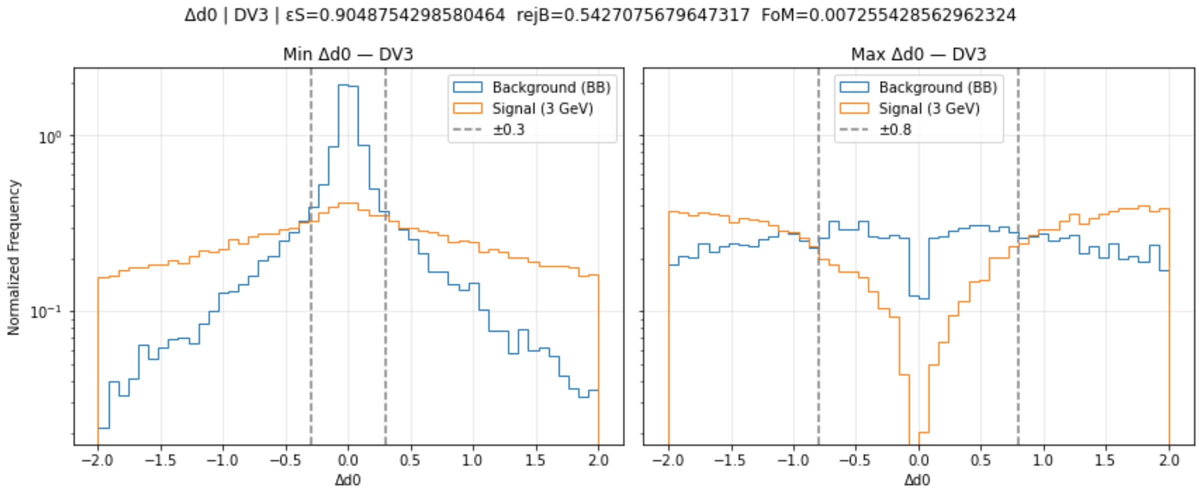

Figure 7.13: Distribution of $\Delta d_{0,\text{min}}$ and $\Delta d_{0,\text{max}}$ for DV3 vertices.

Dominant variables: Δd_0 and Δd_r For Δd_0, the optimal selection obtained from the scan is:

$$\Delta d_{0,\text{min}} > 0.3, \quad \Delta d_{0,\text{max}} > 0.8, \tag{7.16}$$

yielding:

$$\epsilon_S = 0.90, \tag{7.17}$$

$$\text{Background rejection} = 0.54, \tag{7.18}$$

$$\text{FoM} = 7.26 \times 10^{-3}. \tag{7.19}$$

Similarly, for Δd_r:

$$\Delta d_{r,\text{min}} > 0.3, \quad \Delta d_{r,\text{max}} > 0.8, \tag{7.20}$$

with:

$$\epsilon_S = 0.82, \tag{7.21}$$

$$\text{Background rejection} = 0.62, \tag{7.22}$$

$$\text{FoM} = 7.21 \times 10^{-3}. \tag{7.23}$$

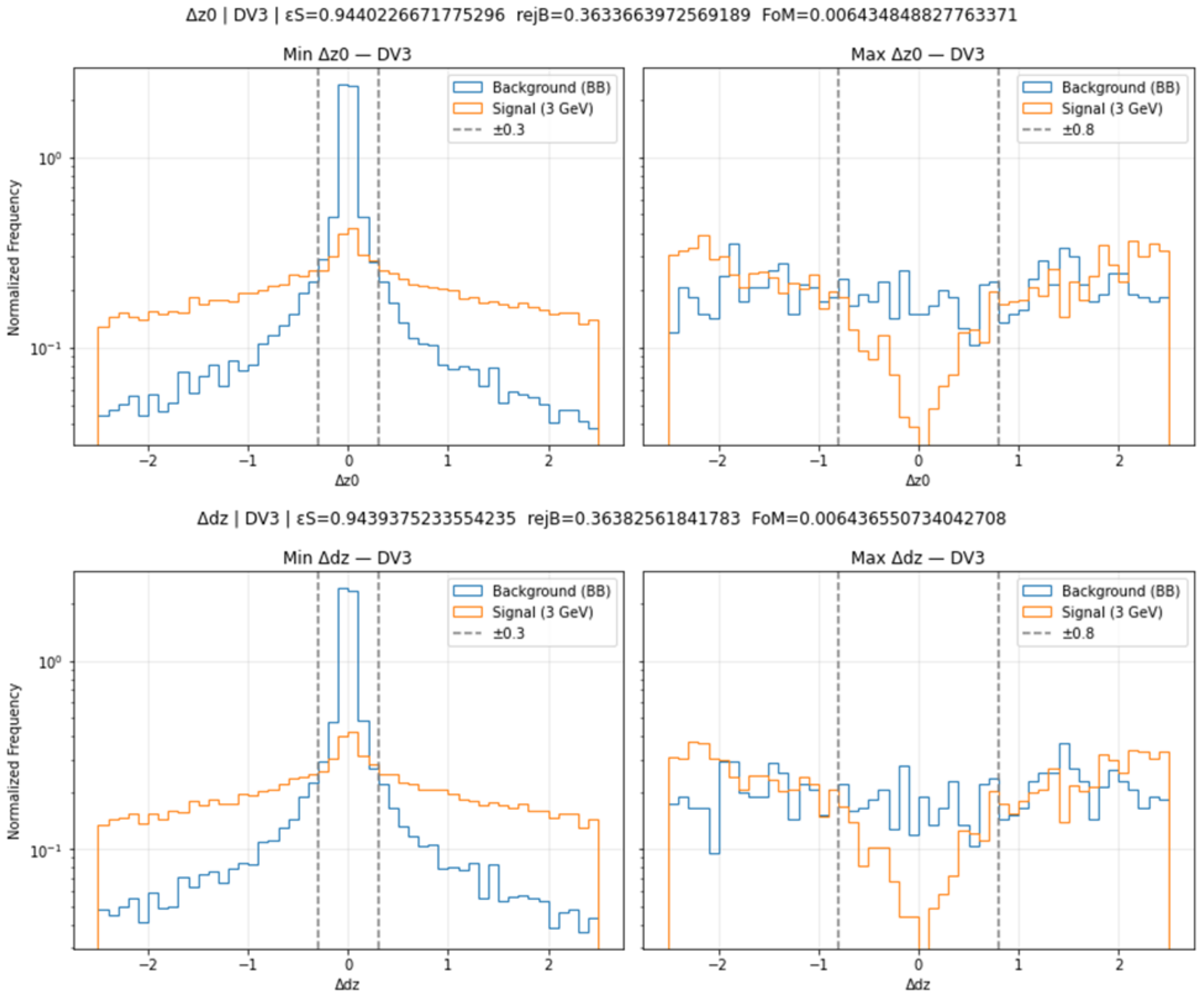

Figure 7.14: Distributions of Δz_0 (left) and Δd_z (right) for DV3 vertices.

Subleading variables: Δz_0 and Δd_z The longitudinal variables show moderate discrimination with the selection:

$$\Delta z_{0,\min} > 0.3, \quad \Delta z_{0,\max} > 0.8, \tag{7.24}$$
$$\Delta d_{z,\min} > 0.3, \quad \Delta d_{z,\max} > 0.8, \tag{7.25}$$

leading to:

$$\epsilon_S \sim 0.94, \tag{7.26}$$
$$\text{Background rejection} \sim 0.36, \tag{7.27}$$
$$\text{FoM} \approx 6.4 \times 10^{-3}. \tag{7.28}$$

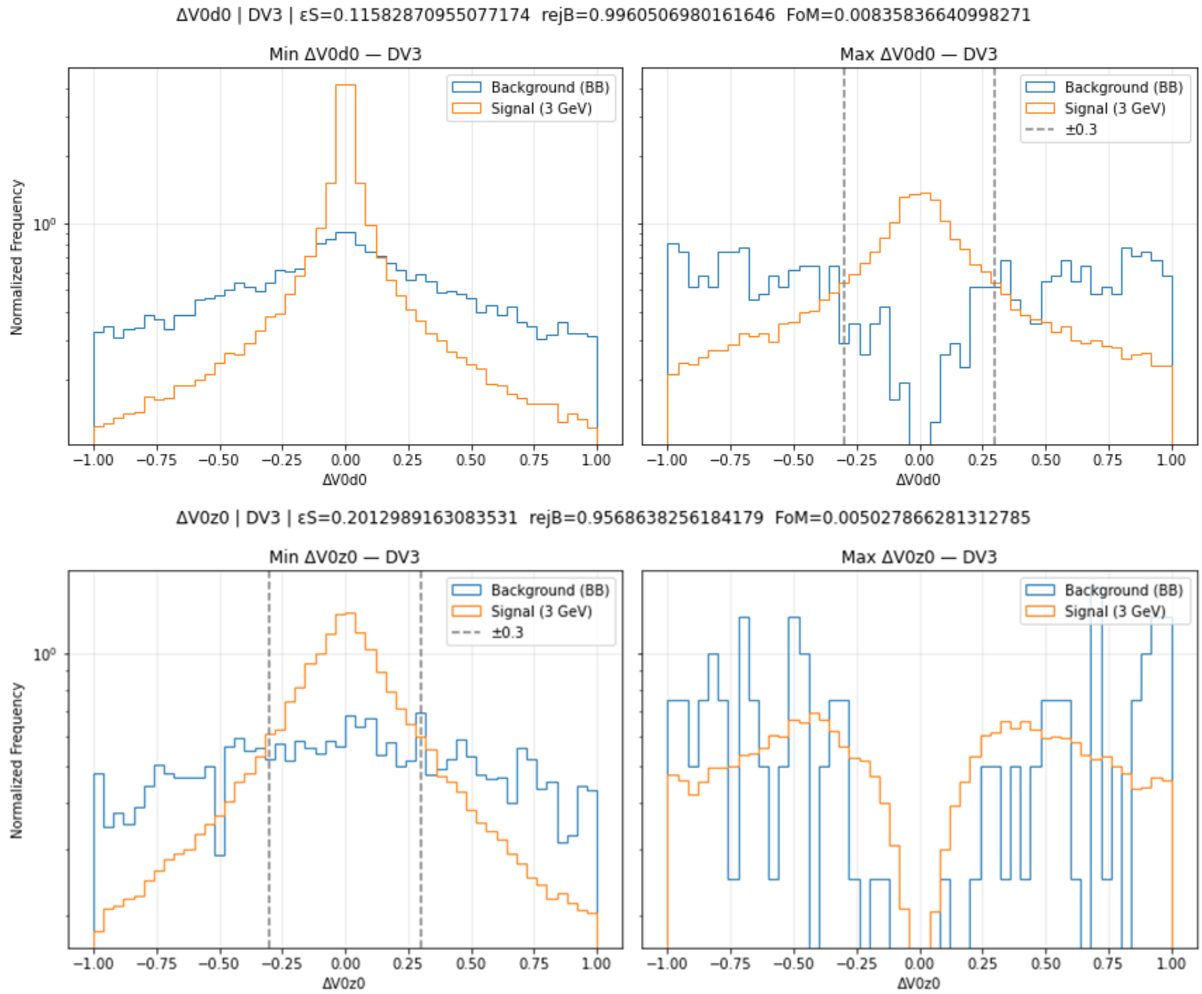

Figure 7.15: Distributions of $\Delta V0d0$ (left) and $\Delta V0z0$ (right) for DV3 vertices.

V0-based variables For V0-related observables, the optimal selection corresponds to the *inside* region, because there is signal peak.

For $\Delta V0d0$:

$$\Delta V0d0_{\text{max}} < 0.3, \tag{7.29}$$

yielding:

$$\epsilon_S = 0.12, \tag{7.30}$$

$$\text{Background rejection} = 0.996, \tag{7.31}$$

$$\text{FoM} = 8.36 \times 10^{-3}. \tag{7.32}$$

For $\Delta V0z0$:

$$\Delta V0z0_{\text{min}} < 0.3 \tag{7.33}$$

with:

$$\epsilon_S = 0.20, \tag{7.34}$$

$$\text{Background rejection} = 0.96, \tag{7.35}$$

$$\text{FoM} = 5.03 \times 10^{-3}. \tag{7.36}$$

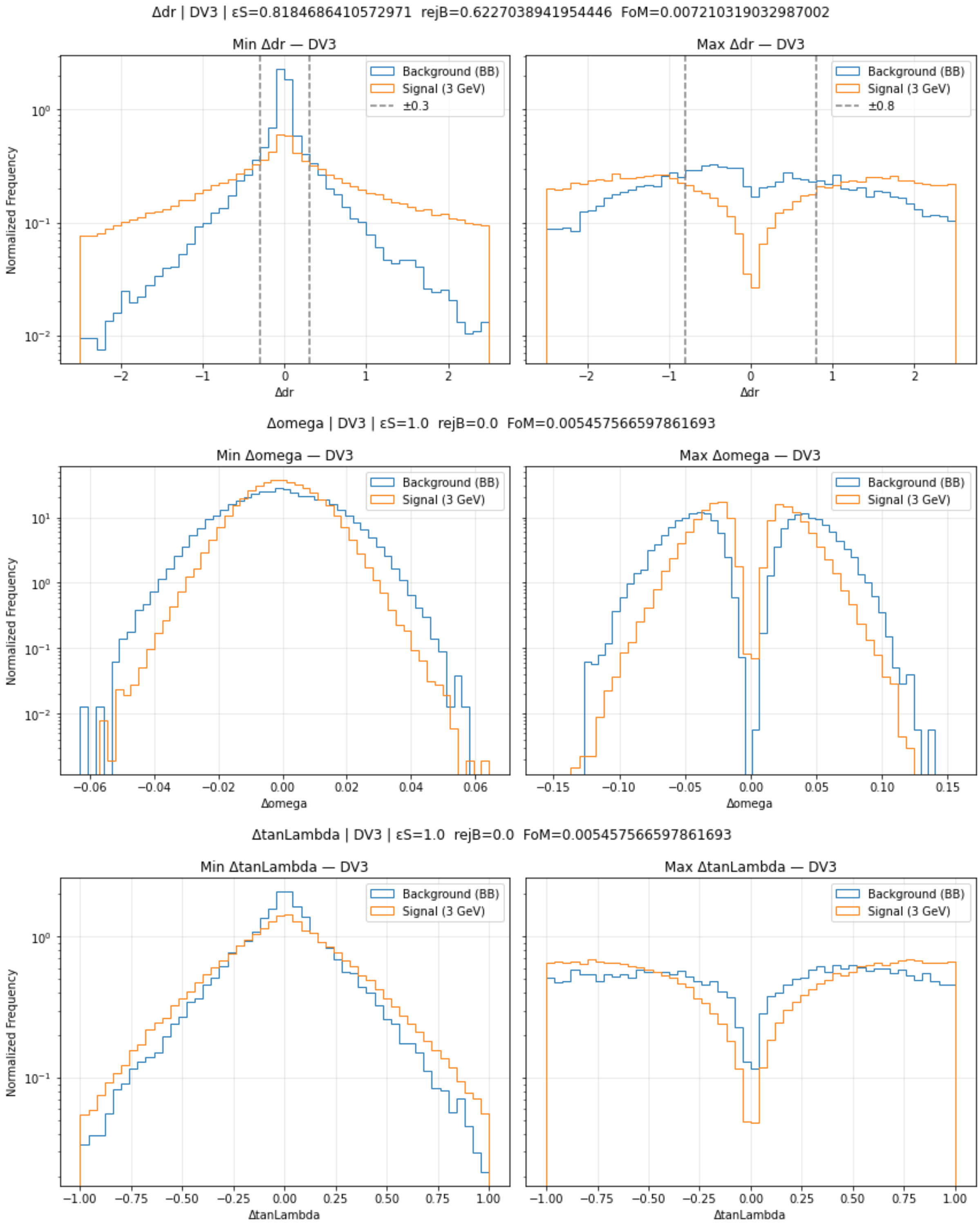

Figure 7.16: Distributions of Δdr, $\Delta\omega$, and $\Delta\tan\lambda$ for DV3 vertices.

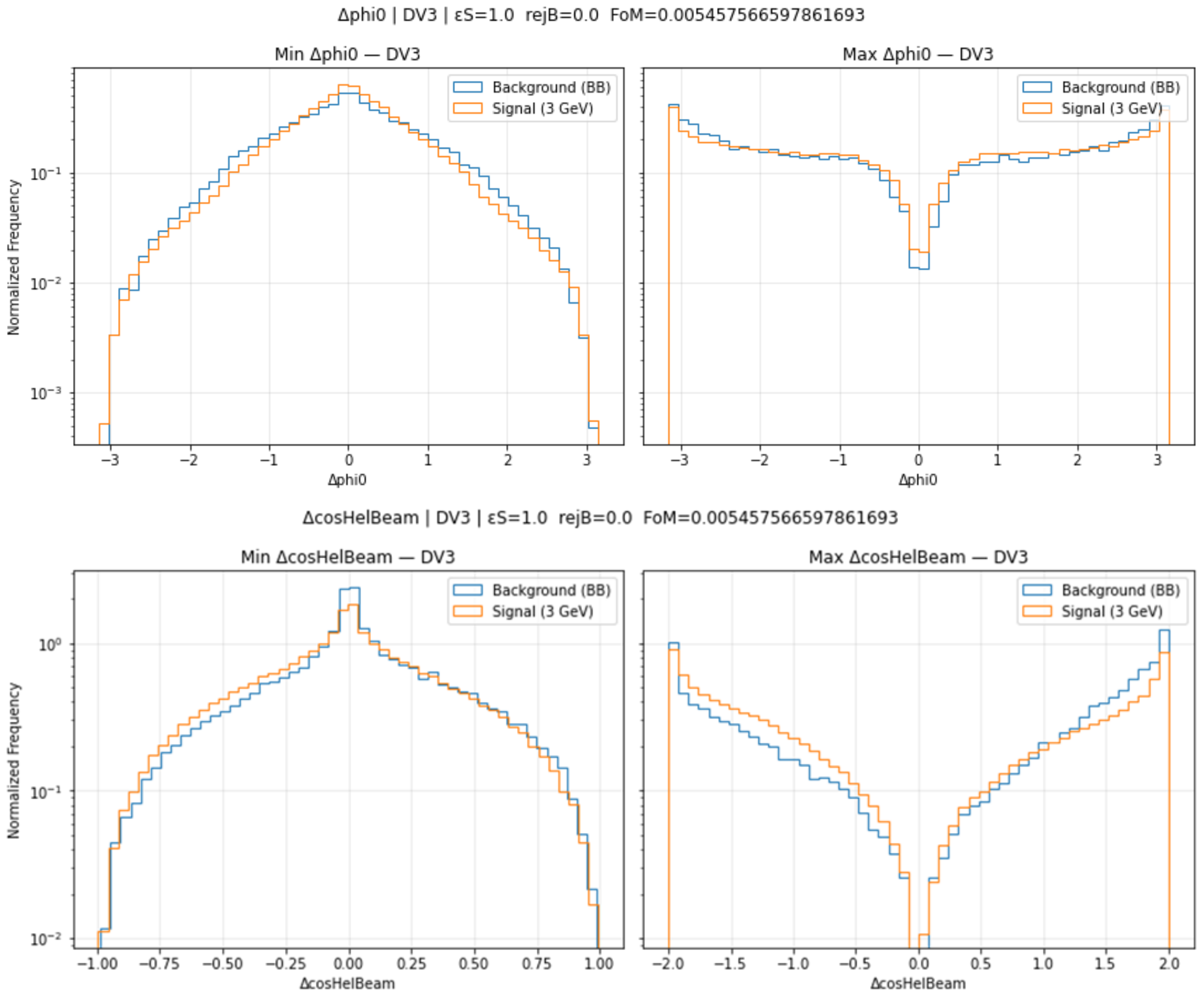

Figure 7.17: Distributions of $\Delta\phi_0$ and $\Delta\cos\theta$ for DV3 vertices.

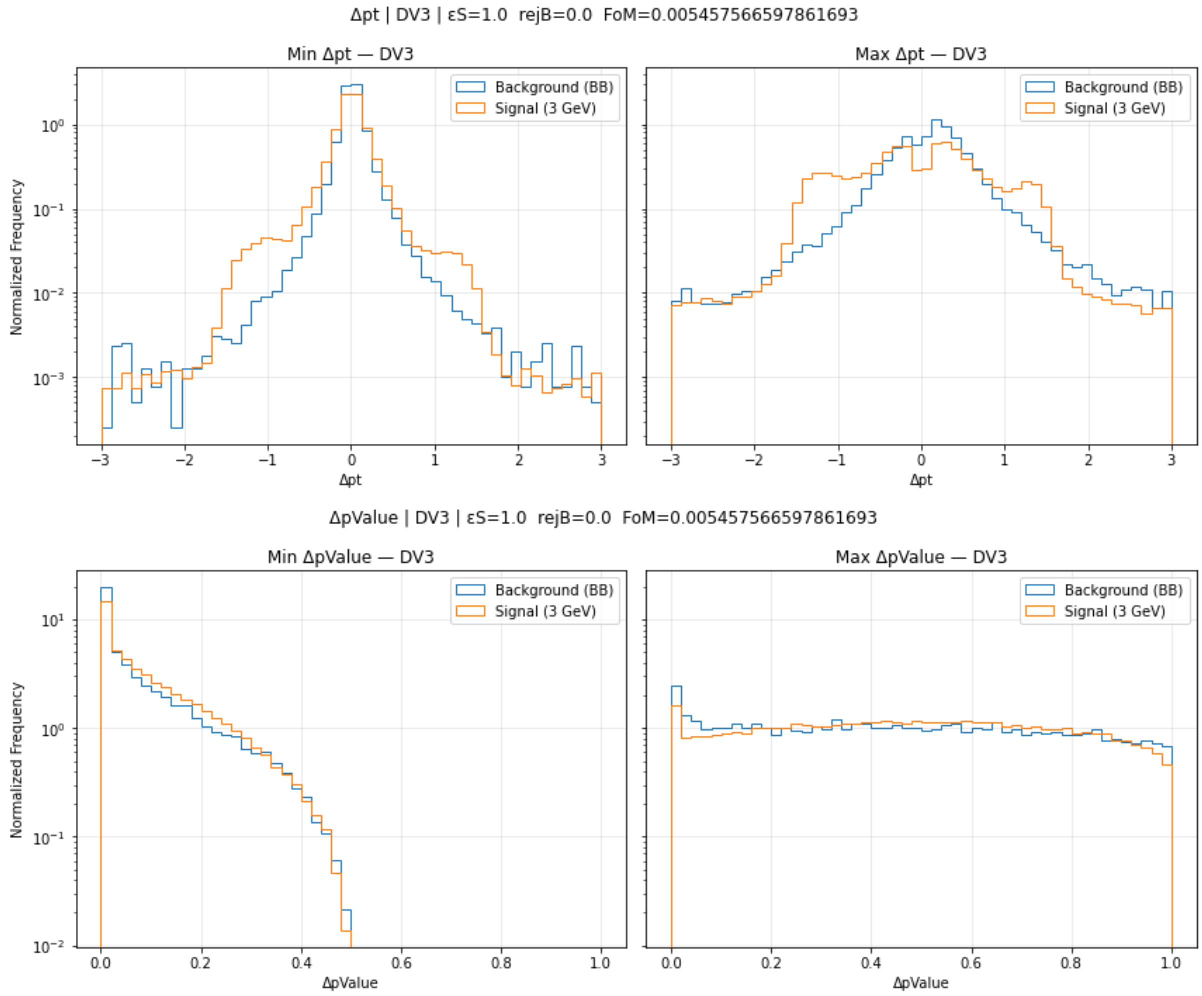

Figure 7.18: Distributions of Δp_T, and Δp-value for DV3 vertices.

Non-discriminating variables All remaining variables shown in 7.16, 7.17 and 7.18:

$$\epsilon_S = 1, \quad \text{Background rejection} = 0. \tag{7.37}$$

Combined performance Combining all variables, the overall selection yields:

$$\epsilon_S^{\text{combined}} = 0.069, \tag{7.38}$$

$$\text{Background rejection}^{\text{combined}} = 0.9997, \tag{7.39}$$

with:

$$\text{FoM} = 1.25 \times 10^{-2}, \quad S/B \approx 1.6 \times 10^3. \tag{7.40}$$

Variable	Cut	ϵ_S	Background rejection	FoM
Δd_0	min > 0.3, max > 0.8	0.90	0.54	7.26×10^{-3}
Δd_r	min > 0.3, max > 0.8	0.82	0.62	7.21×10^{-3}
Δz_0	min > 0.3, max > 0.8	0.94	0.36	6.43×10^{-3}
Δd_z	min > 0.3, max > 0.8	0.94	0.36	6.44×10^{-3}
$\Delta V0d0$	min < 0.3, max < 0.3	0.12	0.996	8.36×10^{-3}
$\Delta V0z0$	min < 0.3, max < 0.3	0.20	0.96	5.03×10^{-3}
Combined	–	0.069	0.9997	1.25×10^{-2}

Table 7.2: Summary of DV3 cut performance.

7.2.3 Higher Track Multiplicity Vertices (DV4-DV6)

For higher track multiplicities, the number of available vertices decreases rapidly. The event statistics for each category are:

$$\text{DV2:} \quad N_{\text{bkg}} = 51227, \quad N_{\text{sig}} = 444112, \tag{7.41}$$

$$\text{DV3:} \quad N_{\text{bkg}} = 32664, \quad N_{\text{sig}} = 211407, \tag{7.42}$$

$$\text{DV4:} \quad N_{\text{bkg}} = 3925, \quad N_{\text{sig}} = 27872, \tag{7.43}$$

$$\text{DV5:} \quad N_{\text{bkg}} = 963, \quad N_{\text{sig}} = 8498, \tag{7.44}$$

$$\text{DV6:} \quad N_{\text{bkg}} = 52, \quad N_{\text{sig}} = 836. \tag{7.45}$$

As the track multiplicity increases, both signal and background statistics drop significantly. In particular, DV4-DV6 suffer from limited statistics, making a robust cut-based optimisation less reliable. Therefore, a detailed analysis for these categories is currently ongoing.

7.3 Data-Driven Estimation of Combinatorial Background

While Monte Carlo simulations provide valuable insights into the expected background from physics aspect. we have to estimate rare occurrences, such as the coincidental crossing of unrelated tracks, can introduce systematic uncertainties. To provide a robust, data-driven estimate of this combinatorial background, an independent evaluation strategy is being employed using populated control regions.

7.3.1 Coincidental Crossing Probability

The core hypothesis of this data-driven method is that the probability of a random track coincidentally crossing an existing vertex to artificially increase its multiplicity is independent of the presence of a prompt baryon in the event.

To quantify this, we define a crossing probability, P_{cross}, which represents the likelihood that a third track coincidentally intersects a genuine two-track vertex to form a fake three-track displaced vertex. We can derive P_{cross} from an inclusive sample of K^0_S mesons, which provides a statistically massive and pure sample of true two-track vertices.

We define the following yields in our control regions:

- $N_2(K^0_S)$: The total number of generic two-track DVs consistent with a K^0_S mass hypothesis.
- $N_3(K^0_S)$: The number of three-track DVs where two of the tracks reconstruct a valid K^0_S. We operate under the assumption that these are truly two-track vertices that have suffered a coincidental crossing from a third, unrelated track.

The coincidental crossing probability is simply the ratio of these yields:

$$P_{\text{cross}} = \frac{N_3(K^0_S)}{N_2(K^0_S)} \tag{7.46}$$

7.3.2 Background Estimation and Validation

With P_{cross} established, we can estimate the number of coincidental-crossing (CC) background events in our signal region. For a three-track DV accompanied by a prompt proton (p), the estimated background yield $N_3^{\text{CC}+p}$ is calculated by scaling the number of two-track DVs (selected in a sideband off the K^0_S mass peak to represent generic background) that are also accompanied by a prompt proton:

$$N_3^{\text{CC}+p} = N_2(\text{off-peak})^{+p} \times P_{\text{cross}} \tag{7.47}$$

To ensure the validity of the independence hypothesis, we test this relation in a highly specific control region. We expect the number of three-track K^0_S vertices accompanied by a prompt proton to follow the exact same scaling relation:

$$N_3(K^0_S)^{+p} = N_2(K^0_S)^{+p} \times P_{\text{cross}} \tag{7.48}$$

Comparing the observed yield of $N_3(K^0_S)^{+p}$ against the prediction from Equation 7.48 serves as a direct closure test for the background model.

In the event that the data statistics are too low to perform this validation with a prompt proton, alternative strategies are outlined:

1. **Particle Substitution:** We can replace the prompt proton requirement with a much more abundant prompt particle, such as a pion (π), and test the relation $N_3(K_S^0)^{+\pi} = N_2(K_S^0)^{+\pi} \times P_{\text{cross}}$.
2. **Kinematic Relaxation:** We can remove stringent event-level kinematic constraints (such as the requirement that the reconstructed invariant mass equation yields a positive discriminant, $D \geq 0$), which artificially suppresses the yields, thereby increasing the available statistics by at least an order of magnitude.
3. **Event Mixing:** If statistics remain insufficient, we can artificially construct background pairs by combining a prompt object from one event with a displaced vertex from a completely different event, effectively removing statistical limitations.

7.3.3 Extension to Higher Multiplicities

The logic applied to the three-track combinatorial background naturally extends to four-track vertices. The number of coincidental-crossing background events featuring a four-track DV and a prompt proton ($N_4^{\text{CC}+p}$) can be estimated by applying the crossing probability to the three-track candidate pool:

$$N_4^{\text{CC}+p} = N_3^{+p} \times P_{\text{cross}} \tag{7.49}$$

Similarly, this can be validated using the K_S^0 control samples by verifying that $N_4(K_S^0)^{+p} = N_3(K_S^0)^{+p} \times P_{\text{cross}}$. This iterative methodology ensures that combinatorial backgrounds are rigorously accounted for across all signal multiplicities purely using data-driven techniques.

Chapter 8

Conclusions and Future Work

This thesis presented the development and implementation of an inclusive search strategy for long-lived light neutralinos produced in B-meson decays via baryon-number-violating R-parity violation at the Belle II experiment. The search targets a displaced vertex signature characterized by multiple charged tracks accompanied by a prompt baryon. The analysis framework establishes the infrastructure for detecting long-lived particles through inclusive displaced vertex reconstruction, specifically addressing highly displaced topologies and high-multiplicity final states.

To evaluate the signal across the phase space of possible neutralino decay topologies, a multi-tiered sample generation strategy was implemented. For neutralino masses between 2.7 and 4.3 GeV, exclusive two-body decay modes were modeled based on $SU(3)$-flavor phenomenological form factor calculations. To generate the higher-multiplicity hadronic final states expected for heavier neutralinos, the Lund string fragmentation model was integrated via Pythia8, using junction fragmentation to handle the baryonic decay topology. The generation of independent samples using the Herwig7 cluster hadronization model is currently in progress. The inclusion of this alternative treatment of color confinement provides a systematic probe of non-perturbative QCD effects, ensuring the sensitivity of the analysis for all scenarios.

Reconstruction algorithms and selection criteria were implemented to identify displaced vertex candidates. A top-down track exclusion algorithm was deployed to reconstruct displaced vertices with track multiplicities ranging from two to six. Combining this algorithm with a TreeFitter-based vertex fitting procedure and iterative track pool managementshould resolve the double-counting problem in combinatorial vertex reconstruction. For vertices located in the Central Drift Chamber region, defined by a radial displacement greater than 16 cm, a particle identification-based mass hypothesis assignment strategy was validated against Monte Carlo truth. This methodology achieves reconstruction efficiencies over 80% for two- and three-track vertices while preserving invariant mass distributions. Residual mass reconstruction biases observed at higher track multiplicities will be addressed in future iterations through neural-network-based particle identification.

The reconstruction framework uses unconventional selection criteria to reconstruct intermediate long-lived neutral hadrons, such as K_S^0 and Λ candidates, as "effective" tracks. Within the intermediate displacement regime of 5 to 24 cm, these criteria yield signal efficiencies over 85% with background rejection rates near 98%, making pool of tracks reasonably pure. Prompt protons and Λ baryons from the primary B decay are identified using beam-constrained mass (M_{bc}) and energy difference (ΔE) requirements to ensure kinematic consistency with the signal topology.

Monte Carlo truth studies indicated that antinucleon annihilations interacting within the beam pipe and the inner wall of the Central Drift Chamber constitute the primary background source for three-track vertices. Analytical estimates show approximately 8% of $B\bar{B}$ events contain an antiproton, producing a statistically significant background at Belle II luminosities. Geometric material maps were constructed for all track multiplicities to apply spatial vetoes. Concurrently, cut-based selections using daughter-track difference variables were developed. For three-track vertices, applying transverse and V0-based spatial cuts demonstrated a background rejection rate of 99.97% with a 6.9% signal efficiency, resulting in a signal-to-background ratio of approximately 1.6×10^3. Currently, optimizing this cuts based on Punzi FOM is going on so that we can retain good amount signal while removing some background, this is already done for effective track analysis, as shown in the 6.3. Extension of these strategies to higher multiplicities is ongoing.

A data-driven framework was designed to estimate coincidental track-crossing backgrounds. using inclusive K_S^0 control samples, the coincidental crossing probability is measured directly from data across multiple kinematic regimes. This provides a background prediction independent of simulation uncertainties, which is required for validation prior to unblinding signal regions.

Future work includes the application of these methods to Belle II collision data collected during Run 1 and Run 2. This involves validation of data quality, hadronic trigger efficiencies, and tracking and vertexing performance as a function of radial position. Background distributions in defined sideband regions will be compared to data to assess the accuracy of the Monte Carlo simulation. Spatial vetoes, potentially using machine learning classifiers trained on hit patterns and energy deposition, will be deployed to mitigate material interaction backgrounds. Systematic uncertainties will be quantified using control samples of known resonances to correct tracking and particle identification efficiencies, and by comparing efficiency distributions between the string and cluster hadronization models.

The inclusive approach pursued in this analysis trades the precision of exclusive reconstruction for increased acceptance, using the e^+e^- collision topology and vertex resolution of the Belle II environment. The reconstruction algorithms, background suppression strategies, and data-driven validation methods are applicable to searches for other long-lived beyond-Standard-Model particles, including heavy neutral leptons, axion-like particles, and dark photons. As the Belle II dataset scales toward the target integrated luminosity of 50 ab^{-1}, this infrastructure will probe the R-parity violating parameter space and provide sensitivity to light, weakly coupled physics at the GeV scale.

Acknowledgements

||જય બહુચર||

I thank my father and mother for their endless support and love. I would like to express my sincere gratitude to my supervisor, Dr. Minakshi Nayak, for her invaluable guidance and support throughout this project. I am also grateful to Prof. Abner Soffer for his guidance on various aspects of the project and for many insightful discussions.

I would like to acknowledge the plots produced by Bogdan Kutsenko, which I have used in this thesis to explain certain parts of the analysis (mentioned alongside the respective figures). I would also like to thank Nayana, Aman Sahoo, and Kumar Rahul for their helpful discussions regarding the Belle II software framework and initial setup.

Bibliography

[1] E. Bertholet et al. "Search for a long-lived neutralino with R-parity violation using an inclusive method". In: (2025). arXiv: 2507.00359 [hep-ph].

[2] Stephen P. Martin. "A Supersymmetry Primer". In: (1997). eprint: hep-ph/9709356.

[3] H. K. Dreiner. "An Introduction to Explicit R-parity Violation". In: (1997). eprint: hep-ph/9707435.

[4] Belle II Collaboration. "The Belle II Technical Detail Report". In: (2010). arXiv: 1011.0352 [physics.ins-det].

[5] Belle II Collaboration. "The Belle II Physics Book". In: (2018). arXiv: 1808.10567 [hep-ex].

[6] Yuki Ohnishi et al. "Accelerator design at SuperKEKB". In: *Progress of Theoretical and Experimental Physics* 2013 (2013). URL: https://api.semanticscholar.org/CorpusID:122906250.

[7] R.L. Workman et al. "Review of Particle Physics". In: *PTEP* 2022 (2022), p. 083C01.

[8] Jochen Schwiening and representing the BABAR-DIRC Collaboration. *DIRC, the Particle Identification System for BABAR*. 2000. arXiv: hep-ex/0010068 [hep-ex]. URL: https://arxiv.org/abs/hep-ex/0010068.

[9] Christian Bierlich et al. "Effects of Overlapping Strings in pp Collisions". In: *JHEP* 03 (2015), p. 148. DOI: 10.1007/JHEP03(2015)148. arXiv: 1412.6259 [hep-ph].

[10] Wouter D. Hulsbergen. "Decay chain fitting with a Kalman filter". In: *Nucl. Instrum. Meth. A* 552 (2005), pp. 566–575. DOI: 10.1016/j.nima.2005.06.078. arXiv: physics/0503191.

[11] Giovanni Punzi. "Sensitivity of searches for new signals and its optimization". In: *eConf* C030908 (2003). Ed. by L. Lyons, R. P. Mount, and R. Reitmeyer, MODT002. arXiv: physics/0308063.

[12] Glen D. Crawford et al. "Measurement of baryon production in B meson decay". In: *Phys. Rev. D* 45 (1992), pp. 752–770. DOI: 10.1103/PhysRevD.45.752.

[13] H. Albrecht et al. “Inclusive production of charged pions, kaons and protons in upsilon (4S) decays”. In: *Z. Phys. C* 58 (1993), pp. 191–198. DOI: 10.1007/BF01560337.